



# Impact of biomass burning aerosols (BBA) on the tropical African climate in an ocean–atmosphere–aerosol coupled climate model

Marc Mallet<sup>1</sup>, Aurore Voldoire<sup>1</sup>, Fabien Solmon<sup>2</sup>, Pierre Nabat<sup>1</sup>, Thomas Drugé<sup>1</sup>, and Romain Roehrig<sup>1</sup>

<sup>1</sup>CNRM, Université de Toulouse, Météo-France, CNRS, Toulouse, France

<sup>2</sup>Laboratoire d'Aérodynamique, Université Toulouse III – Paul Sabatier (UPS), CNRS (UMR 5560), Toulouse, France

**Correspondence:** Marc Mallet (marc.mallet@meteo.fr)

Received: 20 February 2024 – Discussion started: 27 February 2024

Revised: 20 June 2024 – Accepted: 6 August 2024 – Published: 12 November 2024

**Abstract.** The impact of biomass burning aerosols (BBA) emitted in central Africa on the tropical African climate is studied using the ocean–atmosphere global climate model CNRM-CM, including prognostic aerosols. The direct BBA forcing, cloud feedbacks (semi-direct effects), effects on surface solar radiation, atmospheric dynamics and precipitation are analysed for the 1990–2014 period. During the June–July–August (JJA) season, the CNRM-CM simulations reveal a BBA semi-direct effect exerted on low-level clouds with an increase in the cloud fraction of  $\sim 5\%$ – $10\%$  over a large part of the tropical ocean. The positive effect of BBA radiative effects on low-level clouds is found to be mainly due to the sea surface temperature response (decrease of  $\sim 0.5$  K) associated with solar heating at 700 hPa, which increases the lower-tropospheric stability. Over land, results also indicate a positive effect of BBA on the low-cloud fraction, especially for the coastal regions of Gabon and Angola, with a potentially enhanced impact in these coupled simulations that integrates the response (cooling) of the sea surface temperature (SST). In addition to the BBA radiative effect on SST, the ocean–atmosphere coupled simulations highlight that the oceanic temperature response is noticeable (about  $-0.2$  to  $-0.4$  K) down to  $\sim 80$  m depth in JJA between the African coast and  $10^\circ$  W. In parallel to low-level clouds, reductions of  $\sim 5\%$ – $10\%$  are obtained for mid-level clouds over central Africa, mainly due to BBA-induced surface cooling and lower-tropospheric heating inhibiting convection. In terms of cloud optical properties, the BBA radiative effects induced an increase in the optical depth of about  $\sim 2$ – $3$  over the ocean south of the Equator. The result of the BBA direct effect and feedback on tropical clouds modulates the surface solar radiation over the whole of tropical Africa. The strongest surface dimming is over central Africa ( $\sim -30$  W m<sup>-2</sup>), leading to a large reduction in the continental surface temperature (by  $\sim 1$  to 2 K), but the solar radiation at the oceanic surface is also affected up to the Brazilian coast. With respect to the hydrological cycle, the CNRM-CM simulations show a negative effect on precipitation over the western African coast, with a decrease of  $\sim 1$  to 2 mm d<sup>-1</sup>. This study also highlights a persistent impact of BBA radiative effects on low-level clouds (increase in cloud fraction, liquid water content and optical depth) during the September–October–November (SON) period, mainly explained by a residual cooling of sea surface temperature over most of the tropical ocean. In SON, the effect on precipitation is mainly simulated over the Gulf of Guinea, with a reduction of  $\sim 1$  mm d<sup>-1</sup>. As for JJA, the analysis clearly highlights the important role of the slow response of the ocean in SON and confirms the need to use coupled modelling platforms to study the impact of BBA on the tropical African climate.

## 1 Introduction

The southern African savannah is one of the major sources of biomass burning aerosols (BBA) at the global scale, and this region produces about one-third of the carbon emitted by fires worldwide (van der Werf et al., 2010). After their emissions over the continent, the BBA plumes are transported over the south-eastern Atlantic (SEA) during the June to October period every year, modifying the regional energy budget of tropical Africa through different complex mechanisms. First, BBA can interact directly with solar radiation and modify shortwave radiative fluxes at different atmospheric levels (at the surface, within the atmospheric column and at the top of the atmosphere – TOA). Recently, it was shown that BBA emitted over central Africa absorb solar radiation more efficiently than previously thought (Zuidema et al., 2018; Wu et al., 2020; Denjean et al., 2020; Chauvigne et al., 2021). The fact that such absorbing BBA are transported over highly reflective surfaces (low-level clouds) can generate a persistent positive TOA radiative forcing (Meyer et al., 2013; de Graaf et al., 2014; Kacenelenbogen et al., 2019; Mallet et al., 2019, 2020; Solmon et al., 2021) of opposite sign to that generally attributed to anthropogenic aerosols. Currently, global climate models struggle to represent this TOA radiative forcing singularity. Indeed, Mallet et al. (2021) showed that  $\sim 75\%$  of CMIP6 (Coupled Model Intercomparison Project Phase 6) simulations represent a cooling at TOA over SEA due to BBA, because of both an underestimation of the absorbing capacity of BBA and a misrepresentation of the low-cloud fraction. In parallel to the radiative effects simulated at TOA, BBA also significantly reduce the solar radiation reaching the surface, by several tens of Watt per square metre (Sakaeda et al., 2011; Mallet et al., 2019; Solmon et al., 2021). In addition, BBA are now thought to be efficient cloud condensation nuclei (CCN) that can modify cloud microphysical properties, as highlighted by Lu et al. (2018) or more recently by Diamond et al. (2022) over SEA. Finally, the solar radiation absorbed by BBA has been identified as a key process in the BBA impact on low-level clouds over SEA, and several studies using different approaches (models or satellite observations) indicate that BBA tend to increase the cloud fraction (CF) and water content of low-level clouds over SEA through the semi-direct effect (Johnson et al., 2004; Wilcox, 2010; Mallet et al., 2019, 2020; Solmon et al., 2021; Herbert et al., 2020).

By modifying atmospheric thermodynamic profiles, absorbing aerosols also have the capacity to modify the atmospheric dynamics, convection and precipitation at regional and global scales. Samset (2022) indicates that the spread in simulated aerosol absorption in the most recent generation of climate models (Coupled Model Intercomparison Project Phase 6 – CMIP6) can be a dominating cause of uncertainty in simulated precipitation change, globally and regionally. Based on the PDRMIP (Precipitation Driver and Response Model Intercomparison Project) exercise (Myhre

et al., 2017), Samset et al. (2016) indicated that absorbing black carbon (BC) aerosols contribute to the most substantial uncertainties among global climate models in simulating the changes in surface temperature and precipitation. More recently, Persad (2023) argued that tropical regions are particularly sensitive to hydrological-cycle change due to either local or remote aerosol emissions. Uncertainties in the precipitation response are mainly related to the different parameterisations used to represent the physical, chemical and optical aerosol properties and the dynamical processes involved in BC emission from the final radiative impact to the climate impact. The complexity of hydrological feedbacks to the radiative forcing of absorbing aerosols also stems from the fact that this depends on both the so-called “fast” and “slow” responses of the climate system. The fast response is independent of changes in sea surface temperature (SST) and mostly depends on instantaneous modification in atmospheric radiative heating or cooling (O’Gorman et al., 2012). The slow response is mediated by changes in SST and is strongly correlated with TOA radiative forcing. By contrast, the effects of (scattering) sulfate aerosols dominated by the fast response over the tropics are relatively weak (Fig. 3 in Samset et al., 2016).

In parallel to the interactions between desert dust aerosols and the hydrological cycle over tropical Africa (Solmon et al., 2008, 2012; Balkanski et al., 2021), different studies have addressed the impact of BBA plumes emitted over central Africa on cloud properties, atmospheric dynamics and precipitation in the tropics (Lu et al., 2018; Gordon et al., 2018; Diamond et al., 2022; Chaboureaud et al., 2022; Baró Pérez et al., 2024). Solmon et al. (2021) and Ajoku et al. (2019) addressed this issue using regional climate modelling and reanalysis data, respectively, and showed a significant effect, in particular with enhanced drying conditions over southern western Africa. From the methodological point of view, analysis of the various impacts of BBA on radiation, clouds, circulation and the hydrological cycle needs to be addressed using ocean–atmosphere coupled modelling systems so as to enable the ocean surface temperature to respond to the BBA surface radiative forcings. Indeed, the SST response is crucial for understanding feedbacks to the cloud cover (Sakaeda et al., 2011), marine boundary layer dynamics (Mallet et al., 2020) and hydrological cycle (Solmon et al., 2021). At present, most studies that focused on the interaction between BBA and the tropical African climate have used atmosphere-only models in which SSTs are prescribed. A few studies used an atmospheric model coupled to a slab ocean model (Sakaeda et al., 2011; Solmon et al., 2021; Jiang et al., 2020) to investigate the BBA and climate interactions but, as discussed by Solmon et al. (2021), this approach might oversimplify the SST response to smoke aerosols and cloud cover perturbation. The authors state that the use of a fully interactive ocean model will help refine the regional SST response and the associated mechanisms and interactions. Zhao and Suzuki (2019) explored the effects

of black carbon and sulfate aerosols on global and tropical precipitation and emphasised that a slab ocean model overestimates the cross-equatorial heat transport response in the atmosphere as compared with a fully coupled approach. Finally, Lu et al. (2023) recently indicated that the proper assessment of the SST–cloud feedbacks requires fully coupled simulations because the SST changes alter the ocean circulation, which in turn affects SST and clouds.

In this context, the aim of this study is to investigate the interactions between the BBA emitted in central Africa, the radiation budget at the regional scale and the various possible impacts on the tropical African climate using an ocean–atmosphere–aerosol coupled global climate model. This study first focuses on the June–July–August (JJA) season but also examines the impact of BBA in September–October–November (SON), which has been less addressed to date. These two seasons are very important as they are the most intense in terms of emissions from biomass burning in central Africa and also correspond to the development of monsoon in western Africa. This work follows numerous preliminary studies that have tested and largely evaluated the model over this specific region in terms of BBA vertical structure and transport (Mallet et al., 2019; Doherty et al., 2022), aerosol concentrations above low-level clouds (Mallet et al., 2019, 2020; Shinozuka et al., 2020; Redemann et al., 2021; Doherty et al., 2022), induced diabatic heating (Cochrane et al., 2022) and direct or semi-direct effect (SDE) radiative forcing (Mallet et al., 2019, 2020). This study also takes advantage of recent improvements in the representation of optical properties, in particular for the solar absorption induced by BBA (Drugé et al., 2022).

In this context, this study relies on the use of the ocean–atmosphere global climate model (Voldoire et al., 2019), in which an interactive aerosol scheme (TACTIC, Drugé et al., 2022) has been included. This model will be used to investigate in more detail the different impacts of BBA on the tropical African climate. After a detailed description of the modelling methodology (Sect. 2), Sect. 3.1 examines the impact of BBA on cloud macrophysical (cloud fraction) and microphysical (liquid water content) properties as well as the changes in cloud optical properties. The overall effect on the solar surface radiative budget of both the BBA direct effect and changes in tropical clouds is also discussed. In Sect. 3.2, the interaction between the BBA radiative effects, the lower-tropospheric dynamics and precipitation during the JJA season is examined in more detail. Finally, Sect. 3.3 analyses the possible feedback of BBA emissions on radiation, cloud properties and the hydrological cycle during the SON season.

## 2 Method

### 2.1 The CNRM-CM model

The CNRM-CM model is a global climate model developed at CNRM, belonging to a family of coupled ocean–land–

atmosphere climate models that contributed to the CMIP6 intercomparison exercise (Eyring et al., 2016). For CMIP6, two configurations have been used, the CNRM-CM6-1 model (Voldoire et al., 2019), which is the physical core coupled system, and the CNRM-ESM2-1 model (Séférian et al., 2019), which is the Earth system version based on the former with the addition of Earth system components (interactive aerosols, chemistry, carbon cycle and vegetation) and ocean biogeochemistry. In this study, we use a hybrid version: the CNRM-CM6-1 physical core with the addition of the TACTIC aerosol scheme used in CNRM-ESM2-1 (in an updated version published in Drugé et al., 2022). Hereafter this model will simply be named CNRM-CM.

The physical core is composed of the atmospheric global model ARPEGE-Climat V6 (Roehrig et al., 2020), the surface modelling platform SURFEX v8 that notably includes the Interaction Soil-Biosphere-Atmosphere (ISBA) CNRM version of Total Runoff Integrating Pathways (ISBA-CTrip) coupled land surface modelling system, the bulk FLake model (Decharme et al., 2019), the Nucleus for European Modelling of the Ocean (NEMO) v3.6 (Madec et al., 2017) and the sea ice model GELATO (Voldoire et al., 2019). The ECUME (Exchange Coefficients from Unified Multi-campaigns Estimates) iterative approach (Belamari and Pirani, 2007) is used to compute the air–sea turbulent fluxes. The spatial resolution is about 140 km in the atmosphere and land components. In the ocean and sea ice components, the nominal resolution is 1°. ARPEGE-Climat includes 91 vertical levels from the surface to 0.01 hPa in the mesosphere. This global model uses a longwave (LW) radiation scheme based on a rapid radiation transfer model (RRTM, Mlawer et al., 1997) and a shortwave (SW) radiation scheme based on the Fouquart and Morcrette radiation scheme (FMR, Fouquart and Bonnel, 1980, Morcrette et al., 2008) with six spectral bands (whose limits are, respectively, 0.185, 0.25, 0.44, 0.69, 1.19, 2.38 and 4.00  $\mu\text{m}$ ). A detailed description of the physical core component can be found in Voldoire et al. (2019). In this study, the ARPEGE-Climat model includes an interactive aerosol scheme described in the following paragraph.

### 2.2 The TACTIC aerosol scheme

TACTIC is the bulk-bin aerosol scheme used in the CNRM global (Michou et al., 2020) and regional (Nabat et al., 2020) climate models. TACTIC has been developed to represent the main tropospheric aerosol species and their interactions with radiation and clouds. The present work used an updated TACTIC version (Drugé et al., 2022) compared to that of CNRM-ESM2-1 described in detail in Michou et al. (2020). Briefly, the TACTIC aerosol scheme simulates the physical evolution of different aerosol types that are assumed to be externally mixed (particles from different species existing as separate particles): desert dust, sea salt, black carbon, organic matter, brown carbon, sulfate, ammonium and nitrate parti-

cles. Although this represents an important assumption for this region and does not allow possible coating of aerosols during long-distance transport to be represented, the single-scattering albedo (SSA) and solar heating rate have been evaluated (see Sect. 3.1) and are correctly represented in the CNRM-CM model. In parallel, it should also be noted that this representation allows a reasonable computational cost, which is suitable for running long simulations (especially in coupled mode). Finally, further recent developments concerning the formation of sulfate particles, the aerosol wet deposition and the aerosol–radiation coupling are used here and described in Drugé et al. (2022).

More specifically, the TACTIC aerosol scheme includes three size bins for desert dust (central effective radii are 0.1, 0.83 and 5.8  $\mu\text{m}$ , respectively) and sea salt (effective radii of 0.15, 1.9 and 19.1  $\mu\text{m}$ ); two bins (hydrophilic and hydrophobic) of particles for organic matter (OA), brown carbon (BrC) and black carbon (BC); two size bins for nitrates; and one size bin for sulfate ( $\text{SO}_4$ ) and ammonium. All the parameters of the size distribution for organic matter, black carbon, sulfates, fine or coarse nitrate and ammonium are provided in Rémy et al. (2022). In TACTIC, ammonium-nitrate particles are considered hydrophilic (Drugé et al., 2019). Continental biogenic secondary organic aerosols (SOA) are not formed explicitly but are taken into account through the climatology of Dentener et al. (2006), while oceanic biogenic SOA and aromatic SOA are not yet considered. Aerosols can be interactively emitted from the surface (desert dust and sea salt) as a function of surface wind and surface characteristics, or the scheme can consider external emission data sets, including those for anthropogenic and biomass burning particles (BC, OA,  $\text{SO}_2$  and  $\text{NH}_3$ ). As described in Michou et al. (2015), a coefficient of 1.5 is applied to organic carbon emissions in order to take into account the conversion of organic carbon into organic matter. In the present version, the sulfate formation deals explicitly with the chemical oxidation of sulfate precursors into sulfate. In this study, we have used GFED4s (Global Fire Emissions Database) products for the biomass burning emissions (described in van Marle et al., 2017).

The atmospheric model represents the interactions between all aerosols and radiation (direct effect) as well as between hydrophilic particles (OA, BrC, sulfates, ammonium nitrate and sea salt) and cloud albedo (first indirect effect; see Michou et al., 2020, for details). The second indirect aerosol effect, which corresponds to interactions between aerosols and cloud precipitation, is not included. This represents an important limitation, although recent studies of this region seem to indicate that semi-direct effects (absorption and effects on the dynamics) have a greater influence than microphysics. Indeed, Che et al. (2021) showed that the absorption effect of BBA is the most significant on clouds and radiation over SEA using the UK Earth System Model (1.875°  $\times$  1.25° horizontal resolution), which includes the first and second indirect aerosol effects (Mulcahy et al., 2020). They showed that the liquid water path over SEA is significantly enhanced,

mainly due to the solar absorption of the BBA, especially when located above the stratocumulus clouds. In parallel, and using the WRF-Chem-CAM regional model with large eddy simulations, Diamond et al. (2022) indicated a significant increase in cloud cover for a given event when all smoke effects are included, mainly driven by large-scale thermodynamic and dynamic semi-direct effects. Finally, and at the climatic scale, Solmon et al. (2021) showed that the microphysical radiative effect is relatively weak compared to the direct or semi-direct forcings on the cloud and precipitation response (although the authors note that the contribution of the indirect effects should be treated with caution due to a rather simplified representation in climate models). With regards to aerosol–radiation interactions, TACTIC considers the aerosol optical properties (extinction, SSA and asymmetry parameter) detailed in Drugé et al. (2022) for the wavelengths of the radiation scheme. These optical properties depend on relative humidity, except for desert dust, BC and hydrophobic organic aerosol.

### 2.3 Design of the CNRM-CM model configuration

In this study, we intend to estimate the impact of biomass burning aerosols on the ocean–atmosphere coupled system. For this purpose, two simulations, with and without biomass burning aerosol emissions, have been carried out for the 1970–2014 period. However, when including such aerosols, the global mean surface radiative budget is altered, and this modifies the global mean state and in particular the global mean surface temperature. Therefore, it is difficult to disentangle the local effects from feedbacks due to the global mean state change. Here, so as to isolate the local feedbacks, we developed a constrained configuration by nudging the ocean temperature and salinity globally, except in the tropical Atlantic region [26° N–31° S] (see Fig. A1). Both the reference experiment and the sensitivity experiment are nudged towards the temperature and salinity fields of the first member of the CNRM-CM6-1 CMIP6 historical simulation from 1970 to 2014 with a timescale of 6 h and at each ocean level. Both simulations are also initialised in 1970 using the same CMIP6 historical experiment state in 1970. Therefore, both simulations share the same sea surface temperature outside the tropical Atlantic region, and the tropical Atlantic sea surface temperature is not altered by the global mean state change. In summary, the present configuration allows us to focus solely on the ocean–atmosphere feedbacks in the tropical Atlantic, while outside this region the atmospheric model is forced by the same SSTs in each experiment. To disentangle the direct effect of BBA on the atmosphere and the feedbacks resulting from SST changes, three additional SST-forced simulations have been performed. The first two experiments (ATM-ref and ATM-BBA-SST, Table 1) are twin experiments of the coupled experiments, without and with BBA radiative effects where the SST forcing is taken from the respective coupled experiments. The third experiment (ATM-

**Table 1.** Additional SST-forced CNRM-CM simulations. The first two experiments, called ATM-ref and ATM-BBA-SST, are twin experiments of the coupled experiments, without and with BBA radiative effects where the SST forcing is taken from the respective coupled experiments. The third experiment, called ATM-BBA-ref, combines the SST from the ATM-ref experiment and the BBA direct forcing.

CNRM-CM simulation	BBA	Atlantic SST
CPL-ref	No	Coupled
CPL-BBA	Yes	Coupled
ATM-ref	No	SST from CPL-ref
ATM-BBA-ref	Yes	SST from CPL-ref
ATM-BBA-SST	Yes	SST from CPL-BBA

BBA-ref, Table 1) combines the SST from the ATM-ref experiment and the BBA radiative forcing. To summarise, the difference ATM-BBA-ref minus ATM-ref indicates the impact of BBA when SST is fixed, whereas the difference ATM-BBA-SST minus ATM-BBA-ref indicates the additional impact due to the SST change. Both nudged simulations are run over the full period 1970–2014, but the first 20 years are considered a spin-up phase, and we only analyse the period 1990–2014. In the following, the analyses of the CNRM-CM simulations are mainly focused on the coupled configuration, and the additional forced simulations are used to analyse the contribution of the direct radiative forcing of the BBA and the effects due to the change in SST.

### 3 Results

In the results presented hereafter, all the anomalies analysed for the different variables correspond to the differences between the simulations with and without the biomass burning emissions. In addition, the statistical test applied is the Wilk test (Wilks, 2006, 2016) to ensure the robustness of the results.

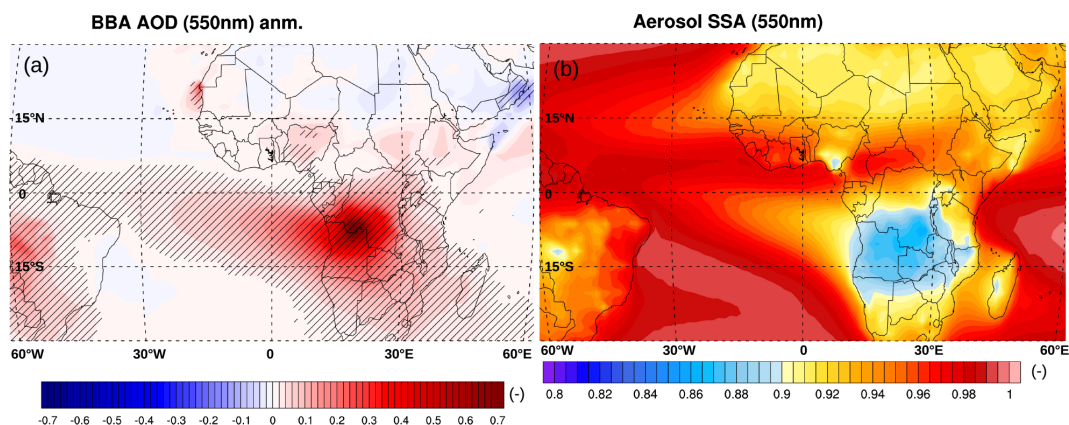
#### 3.1 BBA “radiative perturbations” simulated in the CNRM-CM model

As shown in Fig. 1a, the BBA aerosol optical depth (AOD) anomaly for JJA shows a maximum located over central Africa, with seasonal means reaching  $\sim 0.7$  (at 550 nm). The transport (outflow) of BBA over SEA is also consistent and lies on average between 0 and 15° S. To the west of 30° W, the simulated BBA AOD anomaly is rather low. This regional pattern is in relatively good agreement with the various spatial AOD satellite inversions or reanalysis products, as shown in Mallet et al. (2020). At the global scale, the BBA AOD anomaly is found to be significant over the major BBA source regions such as the Amazon, North America, Indonesia and Siberia (Fig. A1). Some negative AOD anomalies appear locally, especially over the Arabian Peninsula, and are mainly

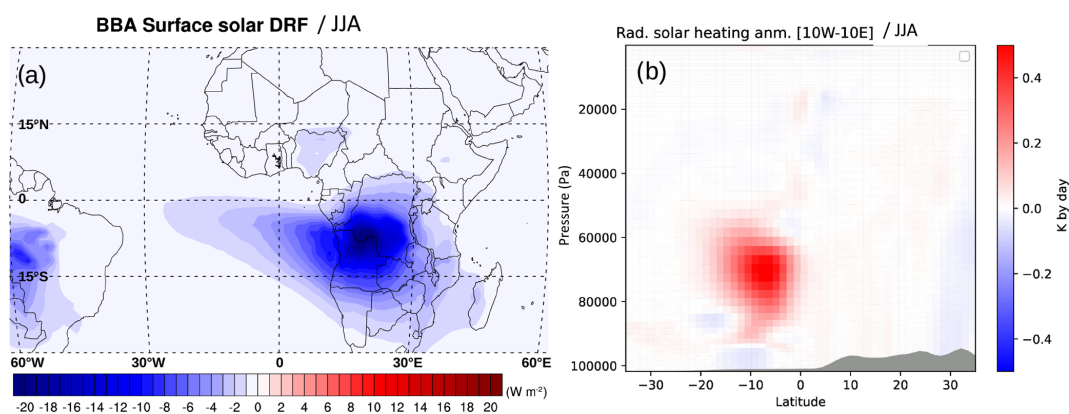
due to negative feedbacks of the BBA radiative forcing on precipitation that favour wet deposition and decreased emissions of mineral dust particles over this region.

Figure 1b also shows that the simulated aerosol SSA over central Africa in JJA is about  $\sim 0.88$  (550 nm) due to the presence of smoke aerosols. This SSA value is consistent with those obtained recently (between  $\sim 0.80$  and  $0.85$  at 550 nm), in particular in the framework of the ORACLES, LASIC, AEROCLO-sA or CLARIFY programs (Zuidema et al., 2018; Wu et al., 2020; Redemann et al., 2021; Chauvigne et al., 2021). In parallel, the SSA of the smoke plumes during the transport over SEA is close to  $\sim 0.90$  (at 550 nm), in agreement with the values reported by Mallet et al. (2021). Figure 1b shows a slightly higher SSA over the Amazon, consistent with the work of Johnson et al. (2016) or, more recently, Holanda et al. (2023).

As shown in Fig. 2a, BBA plumes create a strong radiative disturbance at the surface during the JJA season and significantly decrease the solar radiation reaching the continental and oceanic surfaces. The highest solar direct surface forcing is simulated over areas of high emissions and AOD (Fig. 1a). Over central Africa, the BBA direct radiative forcing reaches seasonal-mean values of  $\sim -10$  to  $-20 \text{ W m}^{-2}$ . The CNRM-CM simulations highlight radiative forcings of  $\sim -5$  to  $-10 \text{ W m}^{-2}$  up to 0° longitude in JJA, with a radiative effect gradually decreasing up to the Brazilian coast, in agreement with the AOD anomaly (Fig. 1a). West of  $\sim 30^\circ \text{ W}$ , the BBA surface forcing is found to be low over the Atlantic Ocean ( $\sim -1$  to  $-2 \text{ W m}^{-2}$ ). The regional pattern of the BBA forcing is consistent with Sakaeda et al. (2011), but some differences in magnitude are observed with higher direct surface forcings (between  $-20$  and  $-40 \text{ W m}^{-2}$ ) in Sakaeda et al. (2011) due to the larger AOD anomaly simulated in this study. The BBA surface radiative forcing simulated in the CNRM-CM model is also consistent with Allen et al. (2019) in terms of regional patterns but has slightly lower values ( $-20 \text{ W m}^{-2}$  over central Africa in Allen et al., 2019). In parallel, Fig. 2b displays the solar JJA heating rate anomaly ( $\text{K d}^{-1}$ ) due to the BBA SW absorption. This radiative perturbation is essential for representing the BBA semi-direct effect on cloud properties (Johnson et al., 2004). As shown in Fig. 2b, the maxima of the solar heating are simulated between 0 and 20° S, with JJA seasonal-mean values of up to  $\sim 0.5 \text{ K d}^{-1}$ . This “heating effect” is mainly confined between 850 and 600 hPa, with maxima at  $\sim 700 \text{ hPa}$ , which corresponds to the altitude of transport of smoke aerosols (Fig. 5a). It should be noted that the solar heating rate simulated in the CNRM-CM model is lower than the values proposed by Wilcox (2010) or Mallet et al. (2020), with seasonal-mean values reaching  $\sim 1$  to  $1.5 \text{ K d}^{-1}$ . This may be due to a slight overestimation of the BBA SSA during the plume transport over SEA. In addition, this difference can possibly be attributed to the underestimation of low-level clouds over the south-eastern Atlantic in the CNRM-CM model (Brient et al., 2019), limiting the re-



**Figure 1.** Averaged (1990–2014) seasonal (June–July–August) (a) anomaly of BBA optical depth (at 550 nm) and (b) effective single-scattering albedo, SSA (at 550 nm), simulated by the CNRM-CM model.



**Figure 2.** Averaged (1990–2014) seasonal (JJA) BBA (a) surface direct radiative forcing ( $\text{W m}^{-2}$ ) and (b) anomaly of the solar heating rate along latitude ( $\text{K d}^{-1}$ , averaged between  $10^{\circ}$  W and  $10^{\circ}$  E).

flection of solar radiation by clouds and hence solar absorption by BBA plumes. Indeed, Feng and Christopher (2015) showed that an increase in the cloud optical depth by about  $\sim 2\text{--}4$  leads to a decrease (of about  $-10 \text{ W m}^{-2}$ ) in the SW direct radiative effect for smoke aerosols (characterised by AOD and SSA of  $\sim 1$  and  $\sim 0.90$  at 550 nm) above clouds at TOA. This reflects the additional solar absorption by the BBA due to higher cloud reflectivity that could then contribute to the enhancement of solar radiative heating by the smoke aerosols.

### 3.2 Effects of BBA on the tropical cloud properties and radiative budget during the JJA season

#### 3.2.1 Changes caused by BBA in the tropical ocean

The impact of the BBA radiative effects on the low-cloud fraction (LCF, %) is shown in Fig. 3a. The CNRM-CM simulations generally show an increase in the LCF in JJA, ranging from  $\sim 5$  to more than 10% over much of the tropical Atlantic. The LCF change maxima are located over the

south-eastern Atlantic, with a positive anomaly higher than  $\sim 10\%$  near the Angolan coast. The BBA effect on the LCF is weaker over the Gulf of Guinea, and the LCF is increased by approximately 5% over this area. In addition to the cloud fraction, Fig. 3b and d also show a BBA effect on the integrated water content and optical depth of liquid clouds over a large part of the Atlantic Ocean. For the water content, the results indicate that the liquid water path (LWP) can be increased by about  $0.006\text{--}0.008 \text{ kg m}^{-2}$  between  $5$  and  $15^{\circ}$  S, with maxima greater than  $0.01 \text{ kg m}^{-2}$  along the coast of Angola (Fig. 3b). However, in contrast to the cloud fraction, the simulated effect over the Gulf of Guinea is found to be small. Figure 3b also shows a decrease in water content in the coastal zones of western Africa, which will be discussed later. Finally, and consistent with the water content, Fig. 3d shows an increase in cloud optical depth (COD) of the order of 1 to 3 between  $5$  and  $15^{\circ}$  S. In addition to BBA surface forcing, this effect on cloud optical properties will contribute to the reduction in solar radiation at the oceanic surface.

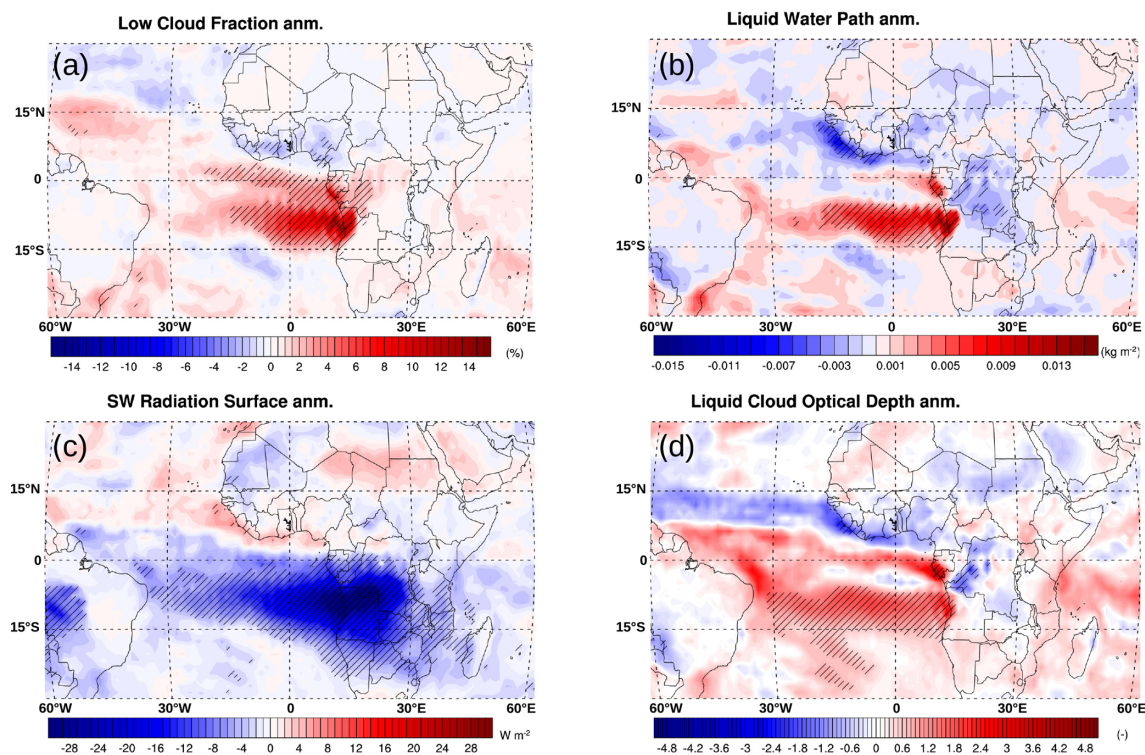


**Figure 3.** Averaged (1990–2014) seasonal JJA anomaly of (a) low-cloud fraction (%), (b) liquid cloud water path ( $\text{kg m}^{-2}$ ), (c) surface downward solar radiation ( $\text{W m}^{-2}$ ) and (d) cloud optical depth, as simulated by the CNRM-CM model. The hatching indicates regions with a significant effect at the 0.05 level (Wilk test).

Over the ocean, the lower-tropospheric stability (LTS, generally defined as the difference in potential temperature between 700 and 1000 hPa, or even SST; Klein and Hartmann, 1993) is known to influence low-level cloud cover (Slingo, 1987). Such studies show a remarkably good correlation between seasonal-mean LTS and low-level cloudiness over the major tropical or subtropical stratocumulus regions, with cloudiness increasing by about 0.05 per 1 K of  $\Delta\text{LTS}$  (Klein and Hartmann, 1993). Over the Atlantic Ocean, the absorption of solar radiation in the atmospheric layer where BBA reside (with the maximum heating occurring at  $\sim 700$  hPa; see Fig. 2b) combined with the decrease in solar radiation and SST (see hereafter) is shown to impact the LTS efficiently. These two processes, detailed in the following, appear to likely be the main causes explaining the changes in cloud properties over the tropical Atlantic.

As shown in Fig. 2a, the BBA radiative direct effects alone contribute to a significant reduction in the solar radiation, reaching both the oceanic and continental surfaces. Over the Atlantic Ocean and between 0 and  $15^\circ\text{S}$ , the combination of the BBA direct forcing and changes in cloud properties (Fig. 3a, b and d) leads to an important decrease in surface solar radiation, with a detectable impact along the Brazilian coast. Figure 3c shows that the simulated solar dimming between the African coast and  $5^\circ\text{W}$  is of the same order of magnitude (between  $-20$  and  $-30 \text{ W m}^{-2}$ ) as in

central Africa near the BBA sources. For longitudes west of  $5^\circ\text{W}$ , the decrease in surface radiation remains significant (between  $-5$  and  $-10 \text{ W m}^{-2}$ ) and is almost exclusively due to the BBA semi-direct effect on low-level clouds (the BBA AOD anomaly is low west of  $5^\circ\text{W}$ , Fig. 1a). This decrease in solar radiation at the ocean surface is slightly offset by an increase in LW radiation (up to  $10 \text{ W m}^{-2}$ ) at the surface due to the higher downwelling LW emissions from clouds related to the positive response of the cloud cover and water content. However, this last effect is mainly concentrated off the coast of Angola (Fig. A2 in the Appendix). The surface dimming simulated over the ocean leads to a regional decrease in SST south of the Equator, with an averaged reduction of about  $\sim 0.3$  to  $0.5 \text{ K}$  during the JJA season (Fig. 4b) and a weaker impact west of  $15^\circ\text{W}$ . It should be noted that this SST effect of the BBA estimated in the CNRM-CM simulations is consistent with the results obtained by Solmon et al. (2021), who used the Regional Climate Model (RegCM) (Giorgi et al., 2023), but it is smaller in magnitude. This could be due to the slab ocean model vs. three-dimensional (3D) oceanic model and the stronger dimming simulated over the ocean in the RegCM model due to higher smoke optical depth and low-cloud response.

In addition to the SST cooling, and as shown in Fig. 2b, BBA transported over SEA generates an additional solar heating of  $\sim 0.5 \text{ K d}^{-1}$  between 600 and 800 hPa due to so-

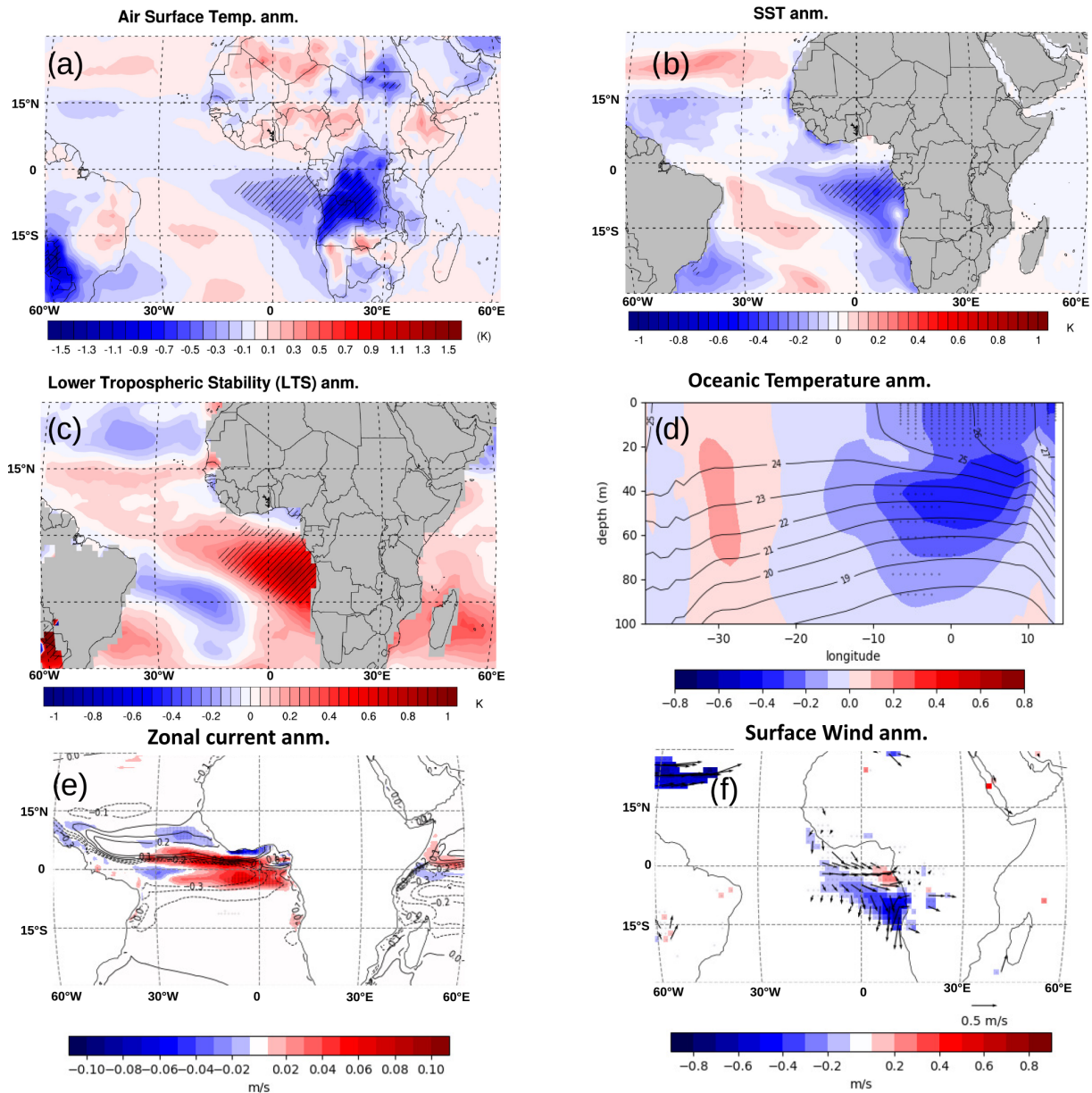


**Figure 4.** Averaged (1990–2014) seasonal JJA anomaly of (a) air surface temperature (K), (b) sea surface temperature (SST, K), (c) lower-tropospheric stability (LTS, K, defined between the surface and 700 hPa), (d) vertical profile of the oceanic temperature along the longitudinal transect from 15° E to 40° W (averaged between 0 and 15° S, K, the isolines representing the climatological values), (e) surface zonal oceanic current ( $\text{m s}^{-1}$ , the isolines representing the climatological values) and (f) the surface wind speed. For panels (a), (b), (c) and (d), the hatching indicates regions with a significant effect at the 0.05 level (Wilk test). For panels (e) and (f), anomalies are only plotted for regions where the statistical test is respected.

lar absorption. Both the solar heating at 600–800 hPa and the SST decrease contribute to increasing the LTS (Fig. 4c). Indeed, the CNRM-CM simulations indicate an important influence of the BBA radiative forcing on the LTS over most of the tropical ocean south of the Equator. The results indicate a strengthening from about  $\sim 0.7$  K near the African coast to  $\sim 0.2$  K up to 15° W. As mentioned previously, this positive impact in the LTS is partly responsible for the increase

in the low-cloud fraction by promoting the stabilisation of the lower troposphere below the aerosol layer (Fig. A3a, b). Indeed, the results indicate a positive anomaly (increase in the subsidence) of the vertical velocity ( $0.01 \text{ Pa s}^{-1}$ ) over the south-eastern Atlantic, especially at 925 hPa. This impact can also be seen in the anomaly of the surface wind amplitude, which is reduced by about  $\sim 0.3$  to  $1 \text{ m s}^{-1}$  over SEA (Fig. A4 in the Appendix). Unlike the low cloud cover, the

effect of the LTS on the LWP is not as direct, as for example in the Gulf of Guinea region, where the effect is smaller even though the LTS also increases (Fig. 4c). In this region, this is due to the compensation between an increase in cloud liquid water content between the surface and 850 hPa and a decrease at 600 hPa (Fig. A5).

This “stabilisation effect” of the lower troposphere is found to be associated with a decrease in the sinking at 700 hPa of about  $\sim 0.01 \text{ Pa s}^{-1}$  between the African coast and  $\sim 10^\circ \text{ W}$  (Figs. 5a and A3f in the Appendix). This is therefore associated with a relative destabilisation in the vicinity of the maximum BBA heating rate (at 700 hPa), resulting in a relative decrease in subsidence (Fig. 5a). These BBA effects are mainly observed between the African coast and  $\sim 10^\circ \text{ W}$ , where the BBA extinction coefficient (at 550 nm) is greater than  $0.025 \text{ km}^{-1}$ . For longitudes west of  $10^\circ \text{ W}$ , the impact on the vertical velocity is small (Fig. 5a). This additional buoyancy generated by BBA heating at these altitudes reduces the descent fluxes above the cloud top, thereby limiting the intrusion of dry air from the free troposphere into the marine boundary layer and contributing to the moistening of the marine boundary layer. Figure 5b clearly shows that the mass fraction of cloud liquid water within the marine boundary layer is increased (by  $\sim 10^{-5} \text{ kg kg}^{-1}$ ) in response to the two main identified processes, explaining the positive impact on the liquid water path and cloud optical depth simulated in the ocean below the Equator (Fig. 3b and d), as discussed previously.

This positive impact of BBA on the low-cloud fraction presents some differences with previous modelling studies using both SST-forced and slab ocean models (Sakaeda et al., 2011; Allen et al., 2019; Mallet et al., 2020; Solmon et al., 2021). Even if the comparisons are obviously not direct due to the differences in the configurations of the models used, the spatial resolutions or the representations of the clouds, comparisons with SST-forced simulations indicate discrepancies, especially over the Gulf of Guinea, where Allen et al. (2019) and Mallet et al. (2020) showed a LCF decrease of opposite sign to the response obtained with the CNRM-CM model. This is found to be consistent with the results indicated in Fig. A6, which shows that the impact on SST clearly affects the low-cloud fraction (increase of up to 5 %) over part of the Gulf of Guinea (GG). In parallel, a source other than the ocean–atmosphere coupling explaining these differences in the response of low-level clouds may be the BBA surface radiative forcing, which is found to be greater over the GG in the SST-forced models, associated with higher solar heating. By contrast, the modelling studies using a slab ocean model (Sakaeda et al., 2011; Mallet et al., 2020) show better agreement with the CNRM-CM model, with a predominantly positive effect over the ocean. However, the amplitude of the low-cloud fraction response is found to be stronger in the coupled model (increase of about  $\sim 10\%$ ) than in the RegCM-Slab Ocean Model (RegCM-SOM) (increase of  $\sim 3\%$ – $5\%$ ), with an impact out to  $15^\circ \text{ W}$  in the

CNRM-CM simulations. Although it is difficult to draw a final conclusion, especially due to the differences between the models, the inclusion of the ocean–atmosphere coupling seems to lead to an increase in low-level clouds over the GG, in contrast to the SST-forced simulations.

Finally, one of the original features of these new ocean–atmosphere coupled simulations concerns the use of the 3D ocean model NEMO. This allows us, for the first time to our knowledge, to study the way in which ocean cooling propagates at depth, in addition to the SST response. Figure 4d clearly shows that the ocean temperature is largely influenced during the JJA season to a depth of about  $\sim 50$ – $60 \text{ m}$  between the coast and  $10^\circ \text{ W}$ . The CNRM-CM simulations indicate a homogeneous cooling between the surface and about  $\sim 20 \text{ m}$  depth, with a temperature anomaly averaging  $\sim 0.3 \text{ K}$ . Figure 4d shows a second cooling zone at greater depths of  $\sim 40$  to  $60 \text{ m}$ , where the negative anomaly may exceed that identified between the surface and  $20 \text{ m}$ . The results also indicate that the cold anomaly propagates to a depth of about  $80 \text{ m}$  during this season. Simulations also indicate an impact on the upper-ocean dynamics (Fig. 4e), where the model simulates a westward equatorial current ( $-0.2$  to  $-0.3 \text{ m s}^{-1}$ ) associated with a counter-current off the coast of western Africa.

In response to the BBA anomaly, the zonal equatorial surface current presents an eastward anomaly, which means a slowing in absolute velocity by  $0.05$  to  $0.1 \text{ m s}^{-1}$  from the African coast to  $20^\circ \text{ W}$ . This “slowing” effect appears to be more intense and spatially more widespread westwards (up to  $30^\circ \text{ W}$ ) north of the Equator than the simulated impact south of the Equator, which is mainly confined between the African coast and  $15^\circ \text{ W}$ . In parallel, the eastward counter-current further north is also slightly weakened, certainly in response to the slowing of the flow at the Equator, although the effect is found to be more limited ( $-0.03 \text{ m s}^{-1}$ ). The most pronounced impact on the counter-current is simulated along the coasts of the Gulf of Guinea, with an effect that can exceed  $-0.05 \text{ m s}^{-1}$ . As shown in Fig. 4f, this slowing of the surface zonal current along the Equator may be due to the surface wind anomaly induced by the radiative effect of BBA. Indeed, the cooling of the SST and the continental temperature near the African coasts, especially that of Angola, generates an anti-cyclonic anomaly (not shown) that favours important changes in wind direction with a more pronounced north-easterly component near the Equator (Fig. 4f). This wind anomaly at the surface may partly explain the slowing of the surface current as simulated in the CNRM-CM model. However, a more detailed analysis of these results related to the change in oceanic temperature and surface dynamics will be carried out in a complementary study.

### 3.2.2 Changes caused by BBA in central and western Africa

Over land, Fig. 3a shows different regional responses of the low-cloud fraction, with impacts mostly positive over cen-

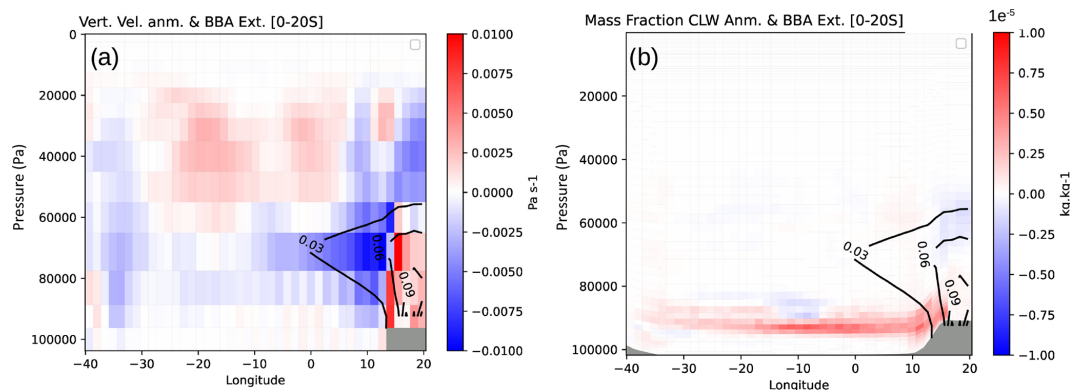


**Figure 5.** Averaged (1990–2014) seasonal JJA anomaly in the vertical velocity vertical profiles along the longitudinal transect from 20° E to 40° W ( $\text{Pa s}^{-1}$ , **a**) and mass fraction of cloud liquid water vertical profiles for a similar longitudinal transect ( $\text{kg kg}^{-1}$ , **b**). Both variables are averaged between 0 and 20° S, and the isolines reported on each transect represent the smoke extinction coefficient at 550 nm ( $\text{km}^{-1}$ ).

tral Africa and slightly negative over western Africa. Over central Africa, the CNRM-CM simulations show an increase in the low-cloud fraction (by more than  $\sim 10\%$ ) over Angola and the coastal region of Gabon, associated with more moderate positive ( $\sim 2\%$  to  $5\%$ ) changes over the Democratic Republic of Congo (DRC). As shown in Fig. A6, the response of the low-level clouds simulated in the coastal areas of Gabon and Angola is not sensitive to the coupling between the ocean and the atmosphere and is probably more related to the increase in moisture advection over this region due to the BBA radiative effect (Figs. A7 and A8) that favours north-westerly anomalies over the ocean south of the Equator (see Sect. 3.3). This contributes to enhancing the low-cloud fraction. The impact on the cloud fraction in the coastal zones of Angola and Gabon appears to be more pronounced in the CNRM-CM simulations than in studies using an SST-forced or slab ocean model approach (Sakaeda et al., 2011; Mallet et al., 2019). In parallel, and over central Africa, the decrease in surface air temperature over the continent (Fig. 4a), in addition to diabatic heating, leads to the stratification of the lower troposphere and limits convection (Fig. 6b), which helps to maintain low cloudiness. In addition to the low-cloud fraction, these new coupled simulations also show an effect on the water content and optical properties of the clouds in central Africa, increasing the liquid water path and cloud optical depth over Gabon and Angola by about  $\sim 0.01 \text{ kg m}^{-2}$  and  $\sim 2$ , respectively. This also contributes to the sharp reduction in solar radiation at the surface simulated over these regions (Fig. 3c).

In addition to the low-level cloud analysis, Fig. 6a shows the BBA impact on mid-level clouds (corresponding to the 785–450 hPa layer) for the JJA period. The results generally show an opposite effect to that obtained for the low-level clouds, with a decrease (by  $\sim 5\%$ – $10\%$ ) in the cloud fraction, especially over central Africa. Over this region, the main processes involved are identical to those discussed previously, i.e. a decrease in the continental surface temperature

associated with radiative heating of the lower troposphere induced by smoke aerosols. Indeed, the significant BBA surface radiative forcing simulated in JJA ( $-20$  or  $-30 \text{ W m}^{-2}$ , Fig. 2a) leads to a large decrease in the surface temperature of about 1 to 1.5 K (Fig. 4a) over a large part of central Africa. This surface cooling, combined with the additional heating due to BBA, induced a more stable lower troposphere below the BBA plumes. As mentioned previously, such effects reduce the vertical ascent and convection, especially between the surface and 700 hPa (Figs. 6b and A3). At such altitudes, the vertical velocity anomaly is about 0.01 to  $0.02 \text{ Pa s}^{-1}$ , reflecting a reduction in the average convection over the continent, especially between 5 and 15° S. As shown in Fig. 6c, the combined effects explain the decrease in the mid-level cloud fraction for atmospheric levels above  $\sim 700$  hPa over central Africa, with a well-marked reduction up to 400 hPa (for latitudes between 5 and 15° S).

Over the central African region, the competing effects between the positive anomaly of the low-cloud fraction (Figs. 3a and 6c) and the mass fraction of cloud liquid water (Fig. 5b) and the negative anomaly of the same variables (Figs. 5b, 6a, c) with respect to mid-level clouds lead to a decrease in the cloud optical depth of the order of  $\sim 1$  (Fig. 3d). Despite this decrease, the BBA direct effect is found to be predominant over this region and explains the significant solar dimming over central Africa (Fig. 3c). Finally, and with regard to high-level clouds, this study shows little impact of the BBA radiative effect on the cloud fraction (Fig. 6c).

### 3.3 How do the BBA affect the lower-tropospheric dynamics and precipitation in JJA?

The impact of the BBA radiative effect on the lower-tropospheric dynamics has been analysed using the wind field at 925 and 850 hPa (Fig. 7). Figure 7a, b first clearly show the south-westerly flow over tropical Africa, which is characteristic of the region and responsible for the develop-

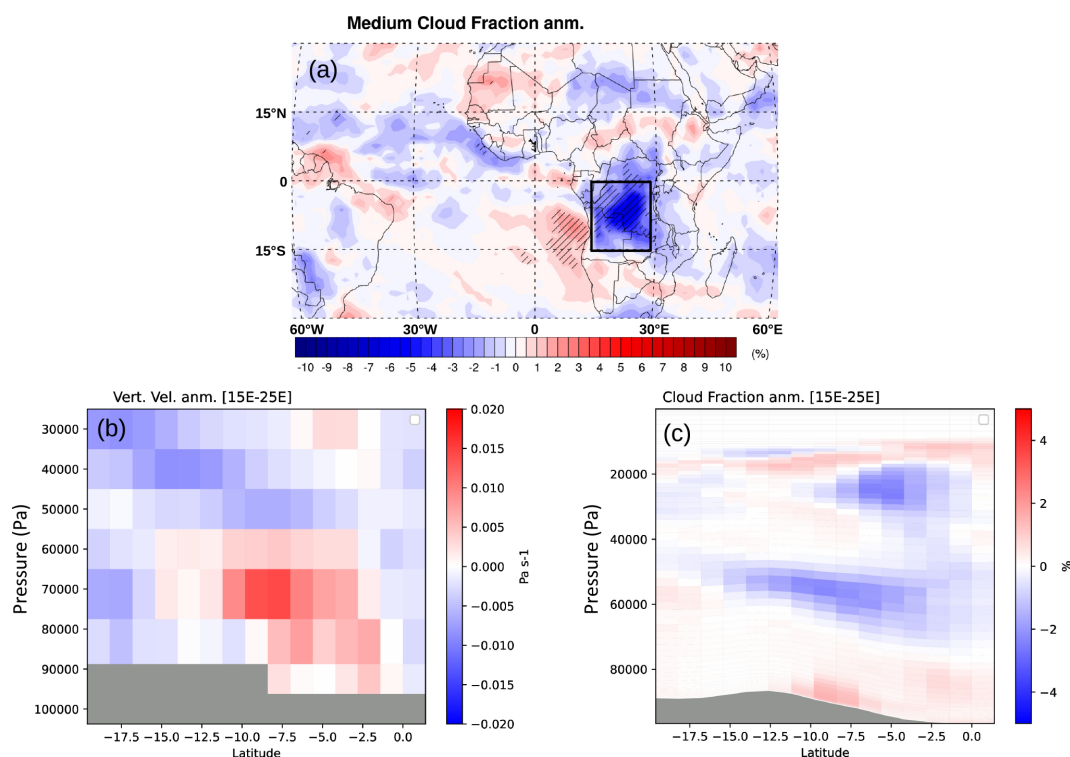


**Figure 6.** Averaged (1990–2014) seasonal JJA anomaly of (a) mid-level cloud fraction (%), (b) latitudinal transect from 5° N to 20° S of cloud fraction vertical profiles (averaged between 15 and 25° E, %) and (c) latitudinal transect of vertical velocity profiles from 5° N to 20° S (averaged between 15 and 25° E, Pa s<sup>-1</sup>).

ment of the western African monsoon in JJA. Near the surface, the results show moderate northerly wind anomalies along the Angolan coast and the Gulf of Guinea (Fig. 7c, d). In addition, Fig. 7 shows a cyclonic anomaly at 850 hPa generated by the BBA radiative effects. The BBA radiative feedback implies wind changes mostly between 15° E and 15° W with north-westerly anomalies over the ocean south of the Equator combined with more northerly anomalies ( $\sim 1 \text{ m s}^{-1}$ ) along the Angolan coast. Hence, and for both heights, the simulated wind anomalies show a general north-westerly flow over the Gulf of Guinea, which opposes the western African monsoon normal flow. As discussed hereafter, the creation of this atmospheric dynamic anomaly at 850 hPa potentially has an impact on the advection of moisture towards central and southern Africa, with implications for rainfall in JJA.

As mentioned in the Introduction section, the hydrological sensitivity to the radiative forcing of absorbing aerosols is very high due to the high complexity of the interactions. The response of precipitation to the forcing of absorbing particles is particularly uncertain over the tropics (Samset et al., 2016; Samset, 2022; Persad, 2023) as such aerosols can exert a rapid adjustment of precipitation in addition to the feedback from surface temperature change (referred to as fast and slow responses, respectively). Figure 8a shows the averaged JJA anomaly ( $\text{mm d}^{-1}$ ) in total precipitation simulated for

the period 1990–2014. The largest negative signal is obtained over the western African coast, with a decrease of about  $\sim 1$  to  $1.5 \text{ mm d}^{-1}$  over the coastal regions of Guinea, Sierra Leone, Côte d’Ivoire, Liberia and Nigeria. On the other hand, there is a moderate positive impact over northern Angola in CNRM-CM simulations. Over this region, the positive effect on the JJA precipitation (increase of  $\sim 0.5 \text{ mm d}^{-1}$ ) is found to be less pronounced than the drying impact simulated over coastal western Africa. It should be remembered here that this effect on precipitation may be underestimated in the simulations, which are biased towards underestimating low-level cloud cover and therefore reflectivity. As mentioned previously, this may lead to an underestimation of the absorption of solar radiation by BBA, radiative heating and hence the simulated cyclonic anomaly and precipitation.

The impact on precipitation over the western African coast and part of the Gulf of Guinea is consistent with the local shift in the convective rain belt towards the south near the Equator as shown in Fig. 8a (in response to the radiative forcing and solar heating exerted in the outflow) and is associated with the 925 and 850 hPa wind anomalies (Fig. 7). This change in the atmospheric dynamics of the lower troposphere tends to decrease relative humidity over the western African coast and increase it south of the Gulf of Guinea (Fig. A4a), which may explain the negative response of precipitation. This drying effect over the western African coast is also

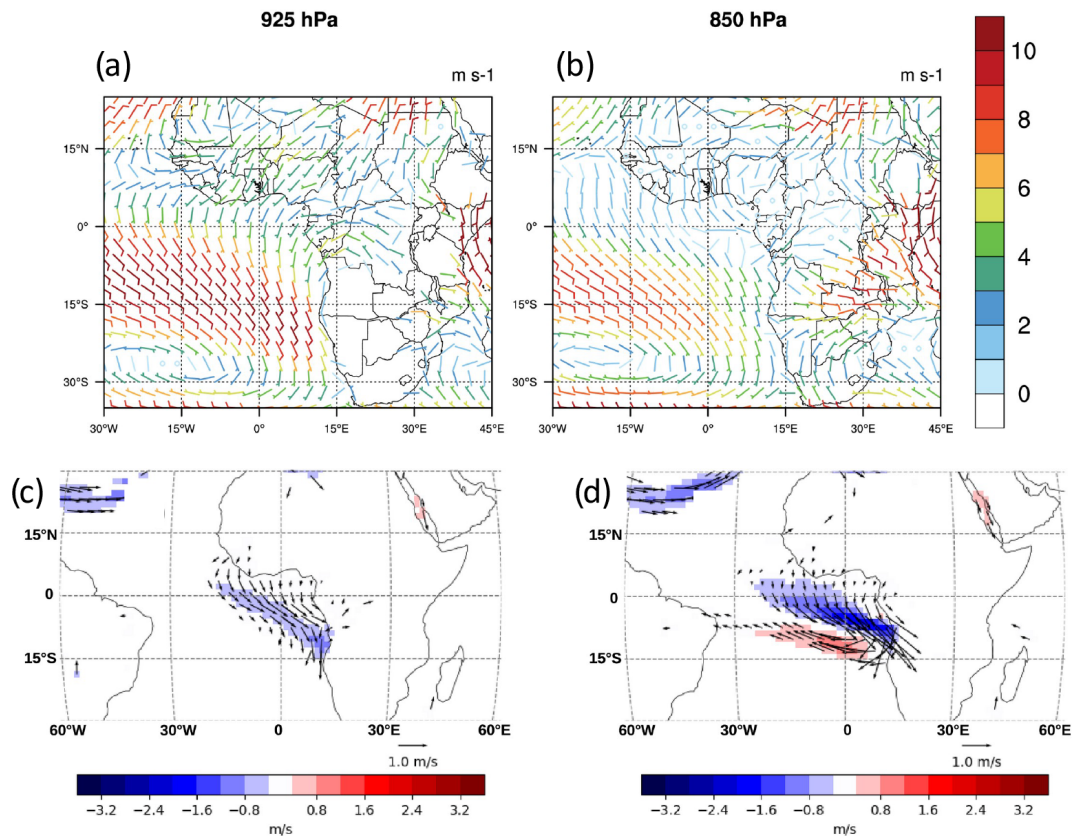


**Figure 7.** Averaged (1990–2014) seasonal JJA wind speed (**a**, **b**) at 925 (**a**, **c**) and 850 (**b**, **d**) hPa ( $\text{m s}^{-1}$ ) and the associated anomalies (**c**, **d**). For the anomalous figures, the significance of the wind field change in both intensity and direction is reported (arrows reported for zones characterised by weak shading indicate that the significance of the wind field change is mainly related to a rotation of the wind).

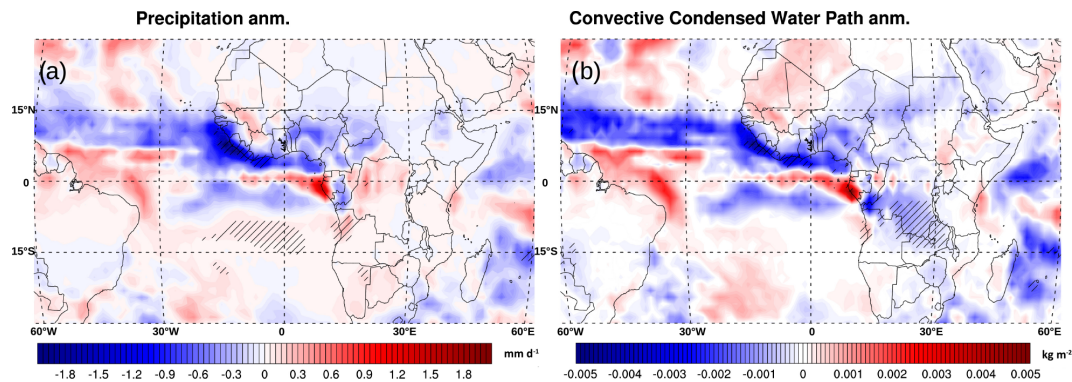


**Figure 8.** Averaged (1990–2014) seasonal JJA anomalies in the (**a**) precipitation ( $\text{mm d}^{-1}$ ) and (**b**) convective condensed water path ( $\text{kg m}^{-2}$ ). Hatching indicates regions with a significant effect at the 0.05 level (Wilk test).

shown in the convective condensed water path anomaly, indicating a decrease from 0.002 to 0.005  $\text{kg m}^{-2}$  over these regions (Fig. 8b). The BBA effect on precipitation simulated by the CNRM-CM model over the oceanic tropical region is found to be consistent with the results of Solmon et al. (2021), who also indicated a general decrease in precipitation (by  $\sim 1.5$  to  $2 \text{ mm d}^{-1}$ ) over this region. However, and

although the overall rainfall response (drying effect) is consistent between the two modelling systems, there are some discrepancies in the regional response, in particular the drying over the coastal regions of Liberia, Sierra Leone and Guinea, which is more important ( $\sim -1.5 \text{ mm d}^{-1}$ ) in this study than the RegCM-SOM simulations ( $\sim -0.6 \text{ mm d}^{-1}$ ). On the other hand, the reduction in rainfall simulated by the

CNRM-CM model in the Gulf of Guinea is less pronounced compared to Solmon et al. (2021). Finally, the hydrological response is opposite over the central African continent, where the RegCM-SOM model mainly simulates a decrease in precipitation, unlike the CNRM-CM model over northern Angola.

Indeed, and as mentioned previously, the CNRM-CM simulations also show a moderate positive ( $\sim 0.3 \text{ mm d}^{-1}$ ) impact on precipitation over northern Angola (Fig. 8a), in agreement with the relative and specific humidity positive anomalies simulated over this region (Fig. A7 in the Appendix). As discussed previously and as shown in Fig. A3 in the Appendix, BBA induce a lower-tropospheric stratification associated with positive vertical velocity anomalies at both 850 and 700 hPa ( $\sim 0.02 \text{ Pa s}^{-1}$ ) that would a priori promote a reduction in the convective rainfall, which is contrary to the positive anomaly simulated in this region. Over central Africa, the moisture advection response to BBA forcings seems to play a role in the moderate increased precipitation. As mentioned above, BBA tend to produce a cyclonic anomaly at 850 hPa over the ocean (Fig. 7b), which then translates into a north-westerly wind anomaly near the coast of Angola that is likely to transport moisture inland (Fig. A7) more efficiently than when favouring precipitation. This hypothesis is supported by the analysis of the vertical profile of the specific humidity tendency anomaly (averaged over the box  $0\text{--}15^\circ \text{ S}$ ,  $15\text{--}25^\circ \text{ E}$ ) for the two terms related to advection and convection (Fig. A8). The results clearly show a positive anomaly above  $\sim 850 \text{ hPa}$  (from  $2$  to  $3 \times 10^{-9} \text{ kg kg}^{-1} \text{ s}^{-1}$ ) for the advection tendency term, while the anomaly for the convective term is found to be smaller. Hence, and as shown for the western African region, the rainfall anomaly observed over Angola seems to be related to the response of atmospheric dynamics and an additional supply of moisture from the Atlantic Ocean.

### 3.4 Response of the tropical African climate to BBA emissions during the SON season

In this part, the analysis focuses on the temporal propagation of the BBA radiative effect for the SON season. This analysis is motivated by the fact that biomass burning emissions, although lower than in JJA, are still present in September–October (Redemann et al., 2021) and would have residual impacts. The interactions between BBA and the tropical African climate are potentially important during this season as SON is characterised by the second phase of the western African monsoon (southward retreat of the rain band from the Sahel to the Guinean coast), with precipitation occurring mainly over the coastal regions (around  $\sim 30$  to  $40 \text{ mm}$  per month) with maxima in October (Maranan et al., 2018).

As shown in Fig. A9 (Appendix), the BBA AOD anomaly simulated by the CNRM-CM model in SON is logically lower than in JJA, consistent with the decrease in biomass burning emissions. The AOD reaches  $\sim 0.3\text{--}0.4$  (at 550 nm)

over the African continent and decreases rapidly to  $\sim 0.05\text{--}0.1$  over the Atlantic. In contrast to JJA, the SON AOD anomaly results in a direct surface forcing that is mainly localised over central Africa ( $\sim -5 \text{ W m}^{-2}$ , Fig. A9), with a weak radiative forcing over the ocean except near the African coast. The simulations show a positive effect of BBA on the low-level cloud fraction, with an increase of  $\sim 5\%$  over the entire tropical ocean and a detectable effect as far as the coast of Brazil (Fig. 9a). Although the impact near the coast of Africa is less pronounced than in JJA, the response is much more widespread in SON, and the effect is remarkable between the Equator and  $15^\circ \text{ S}$ , even though the amount of BBA is lower and mainly restricted to the sources and the African coast. The results indicate the existence of a gradient in the low-cloud response across the ocean basin, with an important effect between  $15^\circ \text{ W}$  and the coast of Brazil compared to the response simulated on SEA. This is partly due to the SST anomaly, which is largest off the Atlantic, with a maximum ( $-0.5 \text{ K}$ ) around  $15^\circ \text{ W}$  (Fig. 10b). This anomaly then affects the surface air temperature up to the coast of Brazil (Fig. 10a). At the same time, the simulations show a slight positive anomaly in the relative humidity over a large part of this region (Fig. A10 in the Appendix), which also contributes to increasing the low-cloud fraction. Figure 9a also shows that the low-cloud fraction over the coastal areas of Gabon is less influenced by biomass burning emissions during the SON season compared to JJA. In terms of the cloud liquid water path, Fig. 9b also shows an increase of about  $\sim 0.005 \text{ kg m}^{-2}$  over most of the oceanic region, except over the Gulf of Guinea, where the simulations indicate a moderate decrease. As noted for the low-cloud fraction, the results clearly show a significant spatial shift compared to JJA and a more pronounced effect compared to the west of the tropical ocean, with a maximum anomaly ( $0.01 \text{ kg m}^{-2}$ ) at about  $30^\circ \text{ W}$ . The overall effect is to increase the liquid cloud optical depth by  $\sim 1$  over the entire oceanic region south of the Equator (Fig. 9c), an effect that is less pronounced than in JJA (Fig. 3b).

The results also show important changes in the cloud properties over part of Brazil, but the present simulations do not allow us to disentangle the contribution of South American emissions from a possible effect of central African emissions. As shown in Fig. A1, the largest AODs due to smoke aerosols in Amazonia are simulated further south of the region where effects on cloud properties are significant. It is therefore possible that the main effects of Amazonian emissions are not related to radiative processes but rather to a change in atmospheric dynamics affecting moisture advection over these regions. In parallel, the contribution of African emissions is not necessarily negligible along the eastern coast of South America. Indeed, as recently reported by Holanda et al. (2023), African smoke could influence aerosol–radiation interactions over the Amazon, with the strongest effect on the eastern basin. This potential impact of BBA over South America will be the subject of a specific study using dedicated simulations.

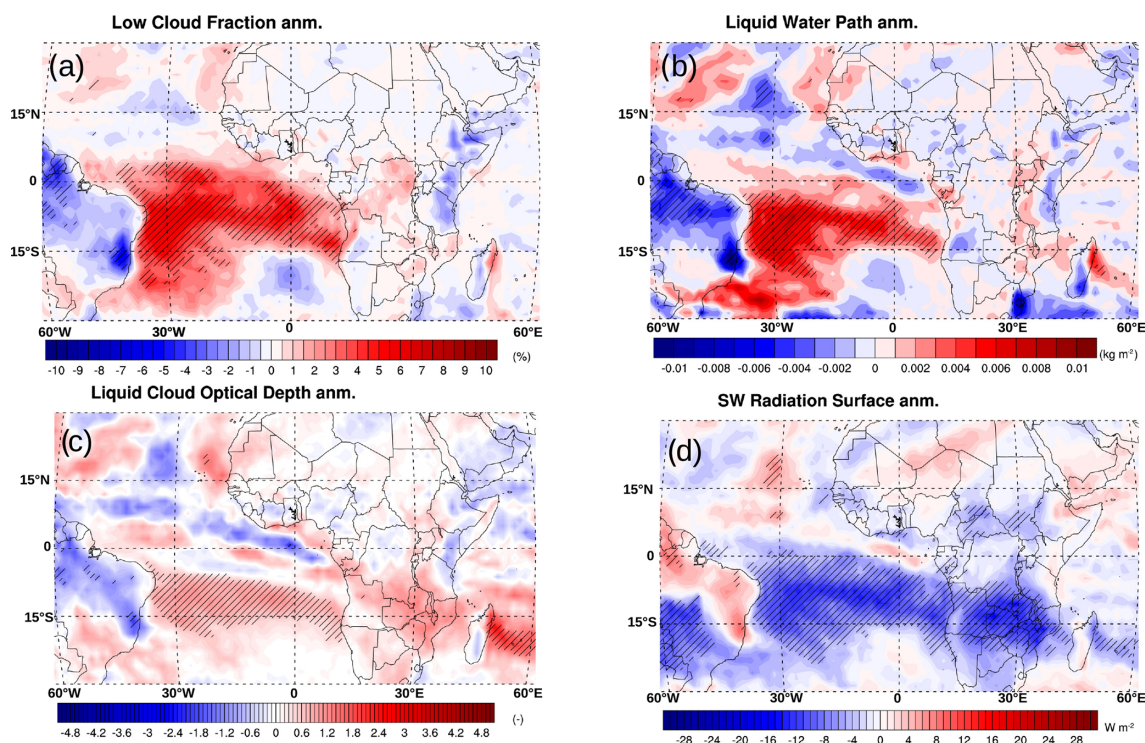


**Figure 9.** Averaged (1990–2014) seasonal September–October–November (SON) anomaly of (a) low-cloud fraction (%), (b) liquid water path ( $\text{kg m}^{-2}$ ), (c) liquid cloud optical depth (no unit) and (d) downward surface solar radiation ( $\text{W m}^{-2}$ ). Hatching indicates regions with a significant effect at the 0.05 level (Wilk test).

In a manner consistent with the BBA AOD and the induced changes in tropical cloud properties, the results indicate important effects on the surface solar radiation in SON. Figure 9d shows a decrease near biomass burning sources of  $\sim 15 \text{ W m}^{-2}$ , combined with a large impact on the ocean south of the Equator. Over the entire oceanic region, from Africa to the coast of Brazil, solar radiation is reduced by  $\sim 10$  to  $15 \text{ W m}^{-2}$ . As shown in Figs. 9a, b, c and A9, this dimming is largely due to the increase in the low-level CF, LWP and COD (mainly controlled by the persistent SST cooling; see the following paragraph), while the BBA direct effect plays a smaller role in this season. In parallel to the changes in clouds and radiation, the results reveal a persistent impact on SST that is still present in SON in the coupled simulations, with a decrease of about 0.5 K over a large part of the tropical ocean (Fig. 10b). In contrast to JJA, the effect is widespread over much of the region, with a decrease simulated over the entire tropical ocean between the Equator and  $15^\circ \text{S}$ . The simulations show that the SST is largely affected between  $0$  and  $30^\circ \text{W}$ , highlighting an influence on a much larger spatial scale than during the period of maximum smoke emission. This SST change is likely due to the strong inertia in the ocean temperature response due to the BBA direct forcing and cloud feedback. Recently, Solmon et al. (2021) also indicated a decrease in the SST between  $0.4$  and  $0.7 \text{ K}$  at  $\sim 5$ – $10^\circ \text{S}$ , but, in contrast to the CNRM-

CM simulations, they reported a more pronounced time lag between the BBA radiative forcing maximum (occurring in August and September) and the maximum in the effects on SST (occurring in October and November). Differences in the low-level cloud response and the ocean parameterisation (oceanic model vs. slab ocean model) may explain the variability in the time evolution of the SST response.

The positive effect on the low-level cloud fraction and liquid water path simulated in SON over the ocean (Fig. 9a, b) is mainly controlled by this persistent SST cooling as shown in Fig. A6. Indeed, the large spatial extension of the cloud response cannot be explained by the BBA forcing itself, which is weaker and mainly confined to the coasts of Africa and  $\sim 5^\circ \text{E}$  in SON (Fig. A6 in the Appendix). As described for the JJA season, the decrease in SST is likely the origin of the increase in LTS (by about  $\sim 0.5 \text{ K}$ , Fig. 10c) and consequently the low-level cloud fraction and integrated water content, indicating that the slow response is also a crucial process in the SON season. In parallel, the simulations show, for the first time to our knowledge, that the ocean cooling is propagated at depth in SON, notably between  $0$  and  $30^\circ \text{W}$  (Fig. 10d). Indeed, the coupled simulations indicate that oceanic temperatures are reduced by  $\sim 0.3 \text{ K}$  down to  $100 \text{ m}$  for latitudes between  $0$  and  $15^\circ \text{S}$ . In addition to the cooling, a positive temperature anomaly is simulated between the coast and  $\sim 5^\circ \text{E}$  between  $\sim 30$  and  $\sim 80 \text{ m}$  depth,

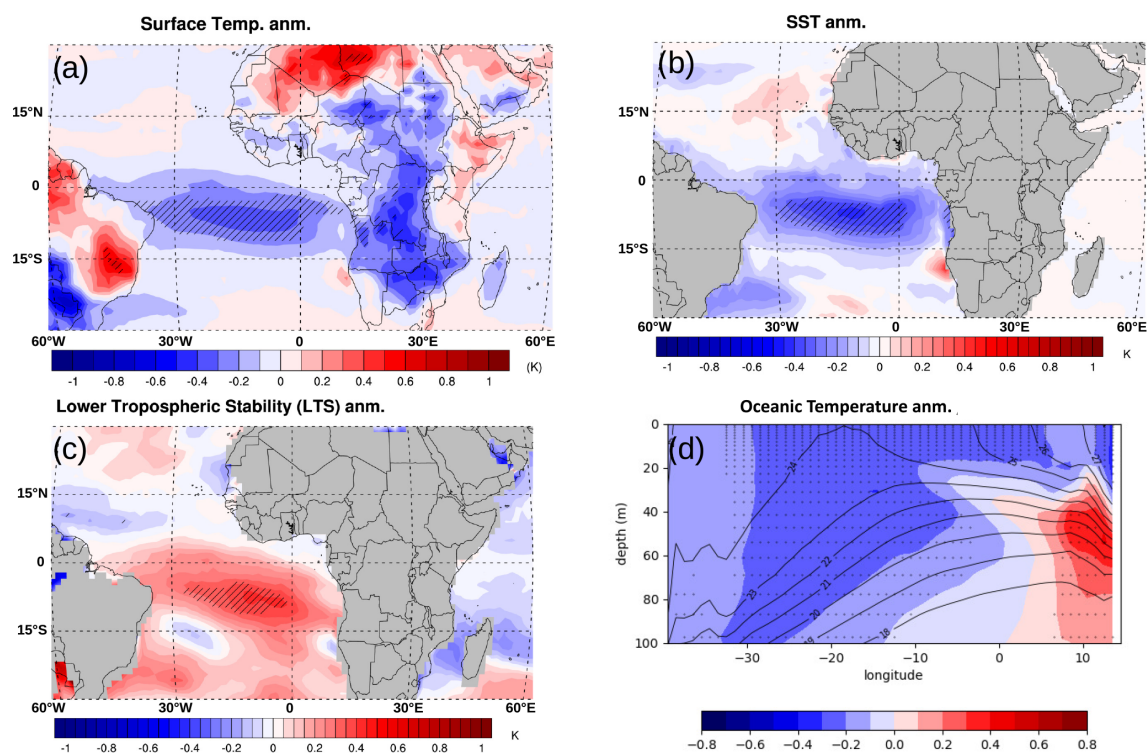


**Figure 10.** Averaged (1990–2014) seasonal SON anomaly of (a) air surface temperature (K), (b) SST (K), (c) LTS (K) and (d) oceanic temperature vertical profiles from 15° S to 40° W (averaged between 0 and 15° S, K). Hatching indicates regions with a significant effect at the 0.05 level (Wilk test).

which could possibly be due to changes in the ocean dynamics. As mentioned above, a specific study will be carried out to analyse the dynamical response and the oceanic temperature changes.

Finally, Fig. 11 shows that the overall impact of BBA radiative forcing on the SON precipitation is mainly observed over the ocean and South America, with no major changes over the African continent. The major impact is localised in the Gulf of Guinea, with a decrease in precipitation of  $\sim 1 \text{ mm d}^{-1}$ . In contrast to JJA, this reduction is more related to the impact of BBA on the SST in SON, which limits convection in the Gulf of Guinea and precipitation. This inhibition is characterised by a reduction in the vertical velocity (Fig. A11 in the Appendix) over this region by about  $\sim 0.005$  to  $0.01 \text{ Pa s}^{-1}$  at 850 and 700 hPa. As shown in Figs. 11 and A11, the maximum reduction in vertical velocity over the Gulf of Guinea corresponds to the regions where precipitation is most affected.

#### 4 Conclusions

The impact of BBA emitted in central Africa on the tropical African climate is studied using the CNRM-CM model in the ocean–atmosphere coupled configuration including an interactive representation of smoke aerosols. The BBA direct and semi-direct effects on clouds, surface solar radiation,

surface–atmosphere flux exchange, atmospheric dynamics and precipitation are analysed first during the JJA season (period 1990–2014). This study indicates an important impact of the BBA radiative effects on the low-level clouds, with an increase in the cloud fraction, water content and optical depth of the order of  $\sim 5\%$ – $10\%$ ,  $\sim 0.01 \text{ kg m}^{-1}$  and  $\sim 1$ – $2$  over the south-eastern Atlantic. Compared to previous studies using global or regional models in an SST-forced configuration, the effect of BBA on the low-level cloud fraction simulated by the coupled CNRM-CM model is found to be more homogeneous and more intense, with a positive impact simulated over the whole of the Atlantic Ocean. This positive impact is found to be mainly due to the BBA radiative effect (especially the lower-tropospheric heating) associated to a lesser extent with the SST decrease (which is in response to the surface BBA radiative forcing of  $\sim -5$  to  $-15 \text{ W m}^{-2}$  and the cloud changes). These both contribute to (i) increasing the LTS and (ii) limiting the intrusion of dry air at the cloud top.

Over land, this study indicates a positive effect of BBA on the low-cloud fraction, liquid water path and optical depth for coastal regions of Gabon and Angola, with a potentially enhanced effect in coupled simulations that integrate the response (cooling) of the SST. In addition, the impact of BBA on the continental mid-level clouds is found to be important during the JJA season, with a reduction of about

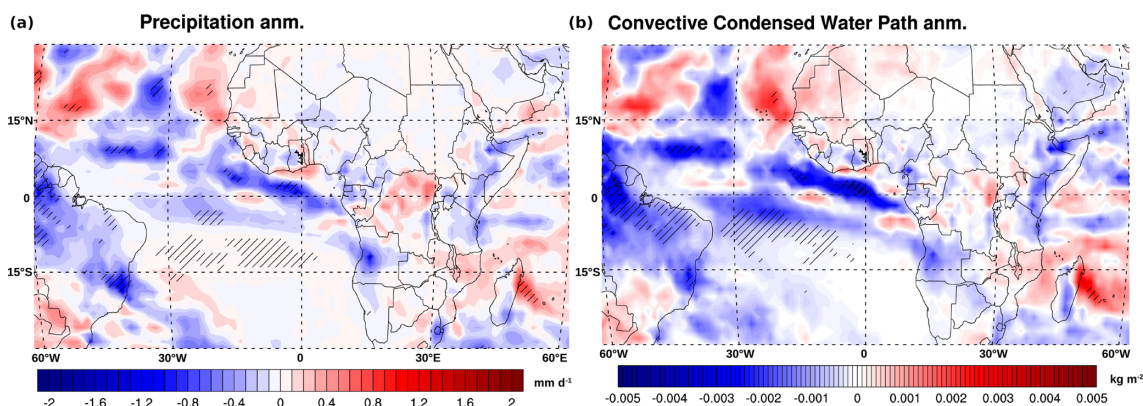


**Figure 11.** Averaged (1990–2014) seasonal SON anomalies in (a) the total precipitation ( $\text{mm d}^{-1}$ ) and (b) convected condensed water path ( $\text{kg m}^{-2}$ ). Hatching indicates regions with a significant effect at the 0.05 level (Wilk test).

10% over central Africa, mostly due to BBA radiative effects inhibiting the convection over the continent. In terms of atmospheric dynamical perturbations, the simulated northwesterly anomalies of winds near the surface and at 850 hPa are found to weaken the western African monsoon flow. The results obtained from these new coupled simulations indicate that changes in the lower-tropospheric dynamics impact the precipitation in JJA, with negative effects over the coastal regions of Liberia, Sierra Leone and Guinea (reduction of  $\sim 1$  to  $1.5 \text{ mm d}^{-1}$ ), associated with a moderate increase over northern Angola ( $\sim 0.3 \text{ mm d}^{-1}$ ).

Another important result is that BBA emissions are shown to have an important effect during the SON season, which is characterised by the second phase of the western African monsoon. Indeed, and despite lower smoke emissions, some large impacts on cloud properties and the radiative budget are still present in SON, which is likely the signature of the slow SST feedback. In particular, the coupled simulations highlight a persistent effect on low-level clouds (increasing CF, LWP and COD) over a large part of the Atlantic Ocean, especially above  $15^\circ \text{W}$ , associated with a precipitation decrease ( $\sim 1 \text{ mm d}^{-1}$ ) over the Gulf of Guinea.

Interestingly, and to our knowledge for the first time, these new coupled CNRM-CM simulations that use a full ocean model (NEMO) have highlighted an impact of BBA radiative effects on the tropical ocean temperature for both studied seasons. The results show that temperatures could be decreased at depths of up to  $\sim 50$ – $80 \text{ m}$  depending on the analysed seasons. Simulations indicate different regional extents of the temperature responses with more limited impact in JJA, which nevertheless corresponds to the maximum of biomass burning emissions. During the SON season, the cooling is simulated at a depth of  $80 \text{ m}$  up to approximately  $30^\circ \text{W}$ , but the general decrease in the ocean temperature is associated with a positive anomaly near the African coast (below  $30 \text{ m}$ ). In parallel to the ocean temperature, the zonal equatorial surface current presents an eastward anomaly, which means a

slowing in absolute velocity (of  $0.05$  to  $0.1 \text{ m s}^{-1}$ ) from the Atlantic coast to  $20^\circ \text{W}$ . This slowing of the surface zonal current along the Equator may be due to the surface wind anomaly induced by the radiative effect of BBA. Following these original initial results, a complementary study will be carried out to look more specifically at the response of the ocean and in particular at the surface currents, density of waters and 3D circulation for both seasons.

Recently, numerous studies clearly demonstrated the important role of the rapid response of tropical precipitation to absorbing aerosols. The present study confirms such results but also highlights that the slow SST response over this tropical region must be considered, as it contributes significantly to the modification of cloud properties, surface radiations, atmospheric dynamics and precipitation. In addition, some of the BBA effects initiated during the dry season can then be propagated to the SON season, mainly due to the inertia of the ocean (cooling) temperature responses. In this sense, the use of coupled models seems to be essential for addressing the different impacts of BBA over this tropical region during the period corresponding to the peak of smoke emissions, but also during other seasons of the year. For example, these new CNRM-CM simulations could also be used to investigate the role of winter emissions which are further north than the study region but which can be transported across the Gulf of Guinea to affect the SST.

The proposed method is a first step towards future modelling exercises that can be improved. First, the present study is only based on the CNRM-CM simulations and could be carried out using different large-scale coupled models, with fixed biomass burning emissions and absorbing optical properties, in order to consolidate the results and better quantify uncertainties. Second, new simulations need to be carried out using a version of the CNRM-CM model that better resolves the low-level clouds over this region. Indeed, this global model, as with most global climate models (GCMs), presents a bias in the representation of these clouds, which

can limit the reflection of solar radiation and possibly lead to underestimation of the BBA radiative heating. As this parameter is crucial for the response of low-level clouds and the atmospheric dynamics over this region, it is possible that the impacts and feedback highlighted in this study would be more pronounced in a version of the model that correctly represents the stratocumulus clouds. In that context, it would be very relevant to carry out a multi-model experiment using different GCMs to quantify these limitations, especially in the response of low clouds, monsoon dynamics and the associated precipitation (and notably the possible drying effect).

Finally, and in order to improve the proposed protocol, additional coupled simulations will be carried out that independently consider only specific tropical emissions (from the Amazon and Indonesia) that could potentially affect this region. These will allow a more detailed analysis of the possible response of tropical Africa's climate to smoke emissions from other regions. In addition, new CNRM-CM simulations will be carried out to analyse the sensitivity of the regional climate response to the absorbing properties of BBA. Finally, the integration of desert dust into future simulations is envisioned to analyse the joint response of the direct and semi-direct radiative impacts of the mixed aerosols on the tropical African climate.

## Appendix A

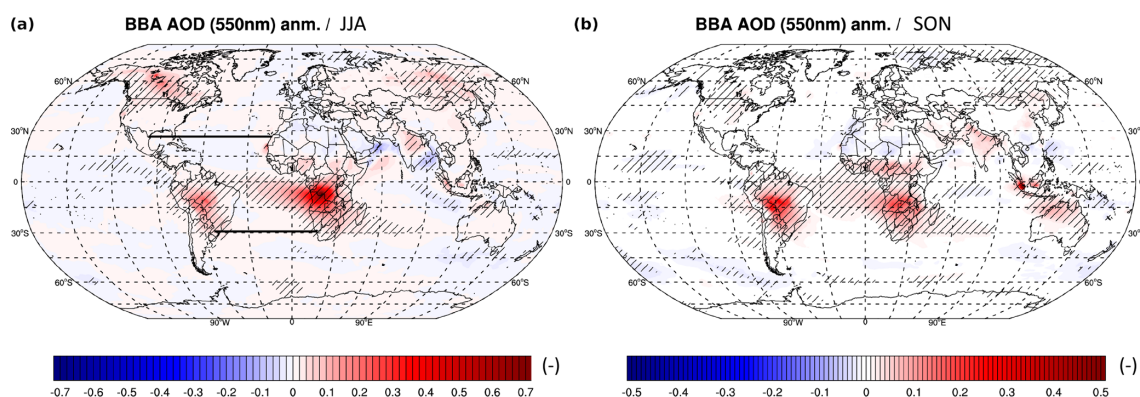


**Figure A1.** Averaged (1990–2014) anomaly of total AOD for the JJA (a) and SON (b) seasons simulated by the CNRM-CM model at the global scale. Hatching indicates regions with a significant effect at the 0.05 level (Wilk test). The latitudinal limits of the oceanic-nudged domain are shown in panel (a).

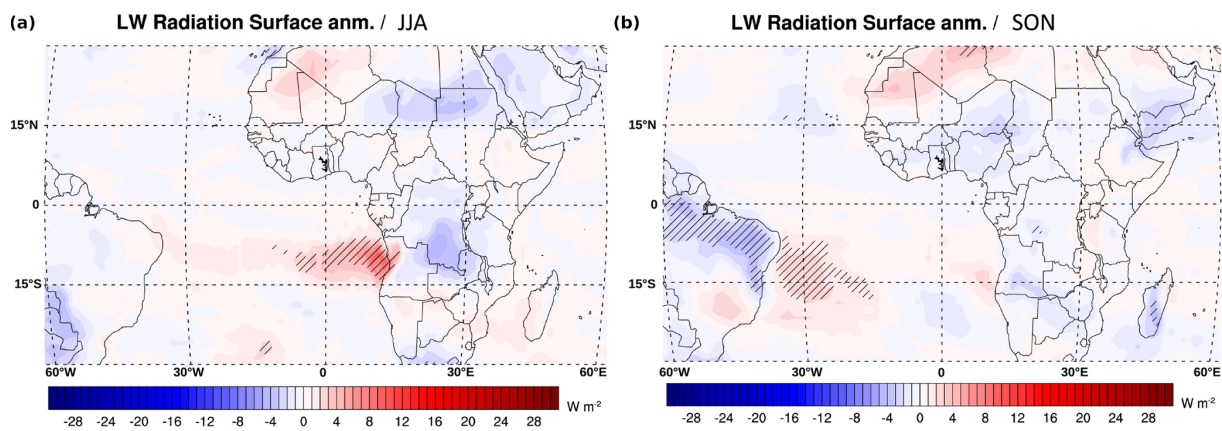


**Figure A2.** Averaged (1990–2014) anomaly of the surface longwave downward radiations for the JJA (a) and SON (b) seasons simulated by the CNRM-CM model. Hatching indicates regions with a significant effect at the 0.05 level (Wilk test).

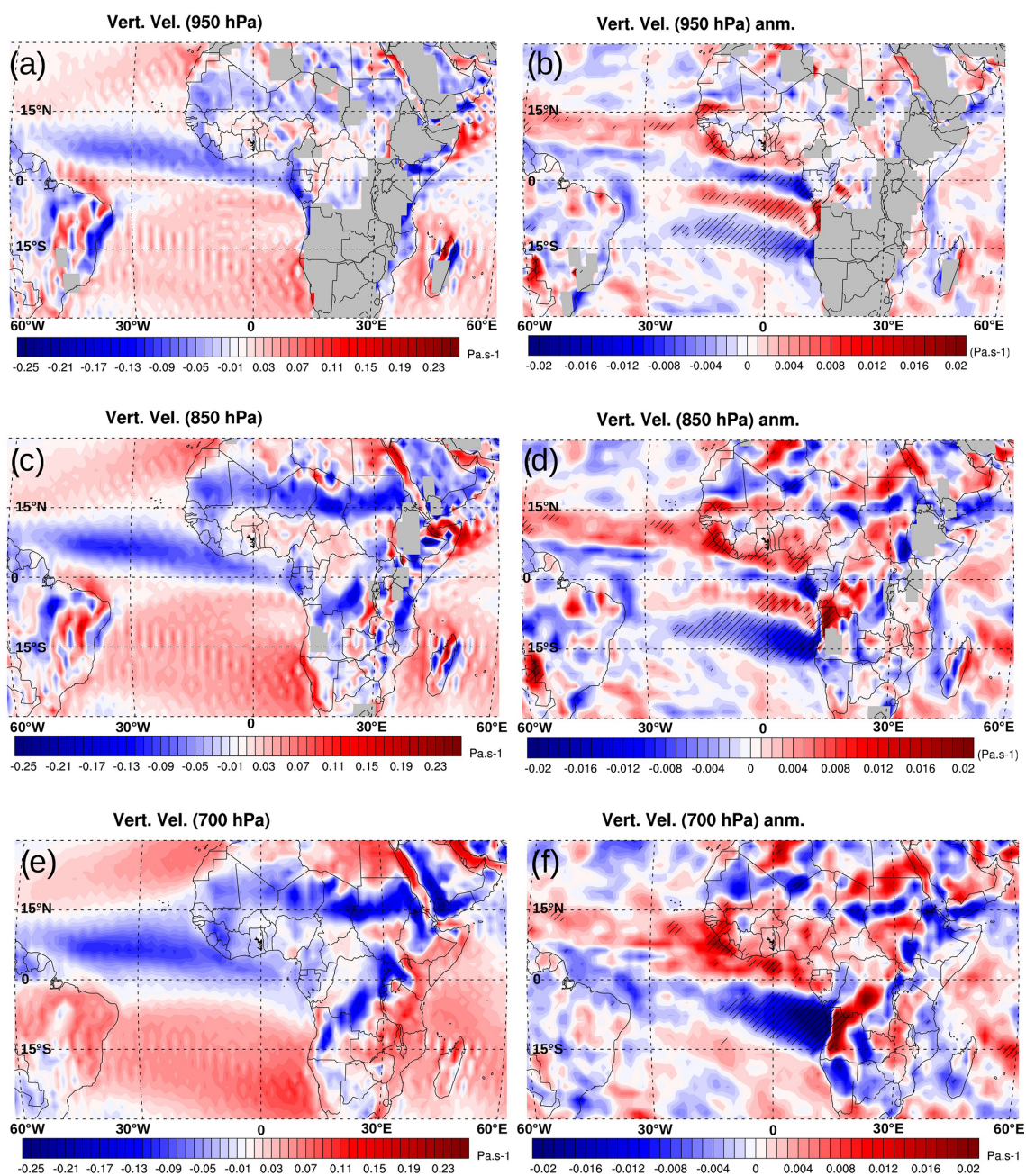


**Figure A3.** Averaged (1990–2014) seasonal (JJA) vertical velocity ( $\text{Pa s}^{-1}$ ) at different altitude levels 950, 850 and 700 hPa (**a**, **c**, **e**) for the CNRM-CM simulations including BBA emissions and the corresponding anomalies (**b**, **d**, **f**). Hatching indicates regions with a significant effect at the 0.05 level (Wilk test).

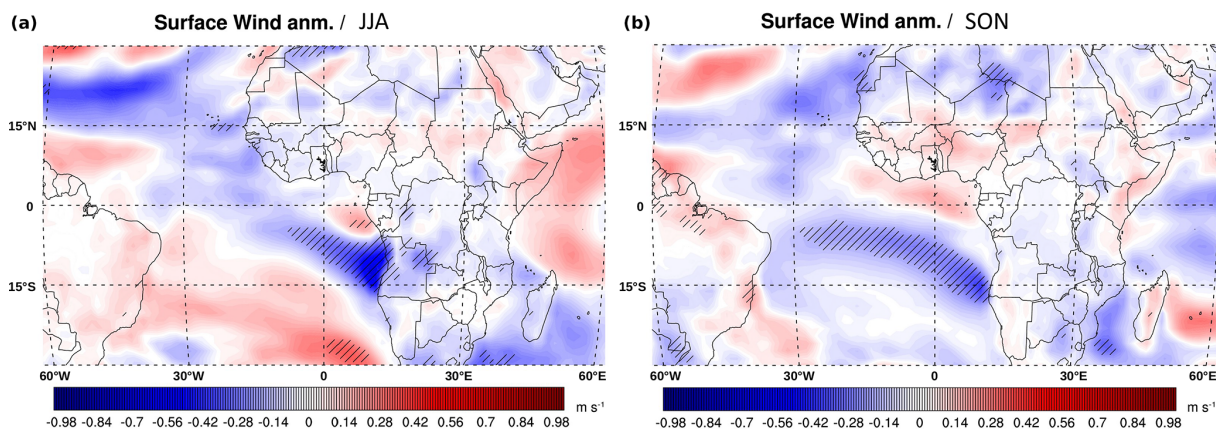


**Figure A4.** Averaged (1990–2014) anomaly of the surface wind ( $\text{m s}^{-1}$ ) for the JJA (**a**) and SON (**b**) seasons simulated by the CNRM-CM model. Hatching indicates regions with a significant effect at the 0.05 level (Wilk test).

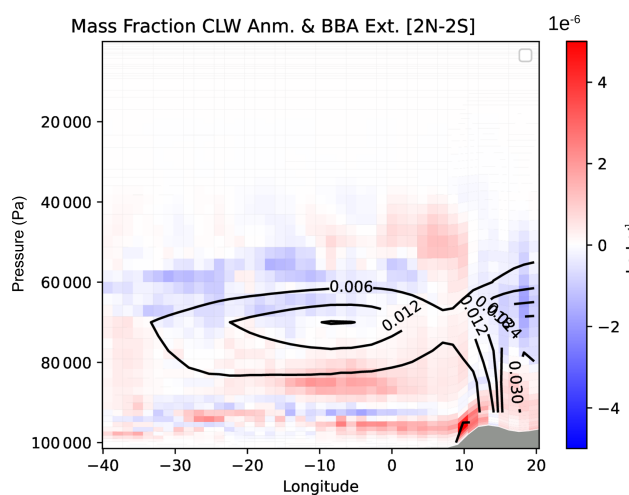


**Figure A5.** Averaged (1990–2014) seasonal (JJA) vertical profiles of the mass fraction of the cloud liquid water anomaly ( $\text{kg kg}^{-1}$ ) for the longitudinal transect averaged between  $2^\circ \text{S}$  and  $2^\circ \text{N}$ .

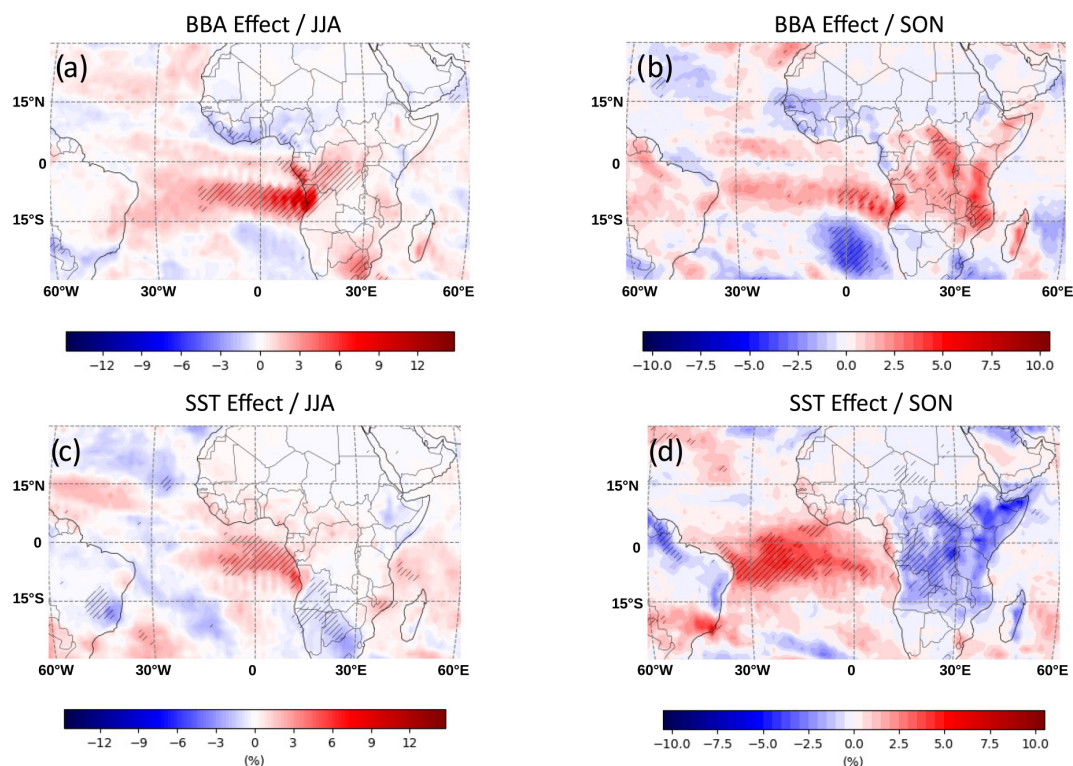


**Figure A6.** Averaged (1990–2014) seasonal anomaly of the low-cloud fraction for the JJA (**a**, **c**) and SON (**b**, **d**) seasons simulated by the CNRM-CM model. Figures (**a**) and (**b**) correspond to the anomaly due to the BBA radiative forcing itself (difference between the ATM-BBA-ref and ATM-ref simulations; see Table 1). Panels (**c**) and (**d**) correspond to the additional anomaly due to the SST changes (difference between ATM-BBA-SST and ATM-BBA-ref, Table 1). Hatching indicates regions with a significant effect at the 0.05 level (Wilk test).

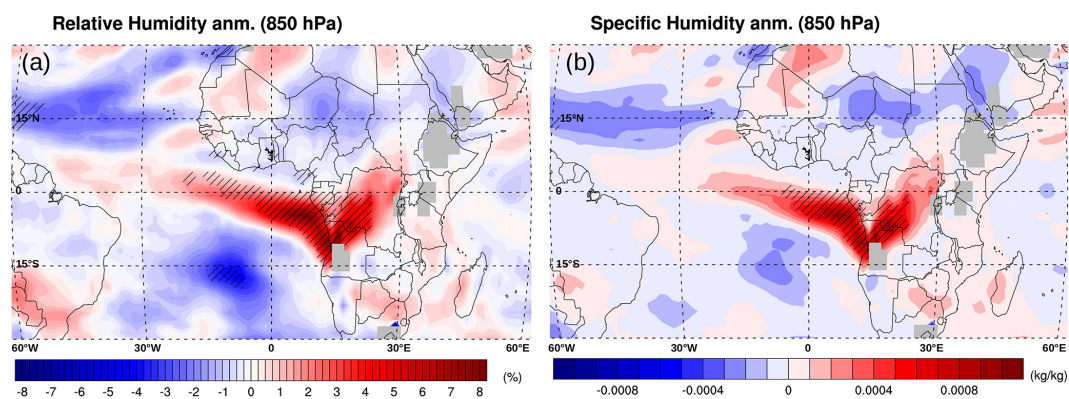


**Figure A7.** Averaged (1990–2014) seasonal (JJA) anomaly of the (**a**) relative humidity (%) and (**b**) specific humidity ( $\text{kg kg}^{-1}$ ) (at 850 hPa) simulated by the CNRM-CM model. Hatching indicates regions with a significant effect at the 0.05 level (Wilk test).

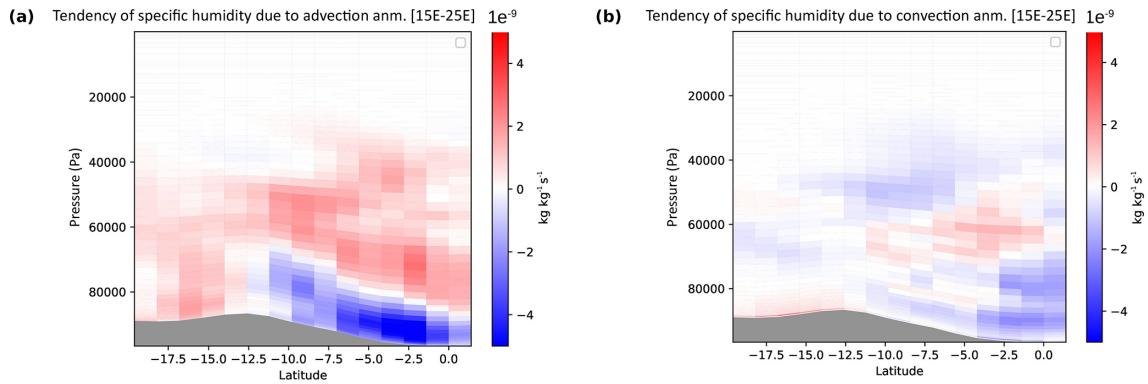


**Figure A8.** Averaged (1990–2014) seasonal (JJA) anomaly of the latitudinal transect, from  $5^{\circ}$  N to  $20^{\circ}$  S, of the specific humidity trends due to the advection (a) and convection (b) ( $\text{kg kg}^{-1} \text{s}^{-1}$ , averaged between  $15$  and  $25^{\circ}$  E).

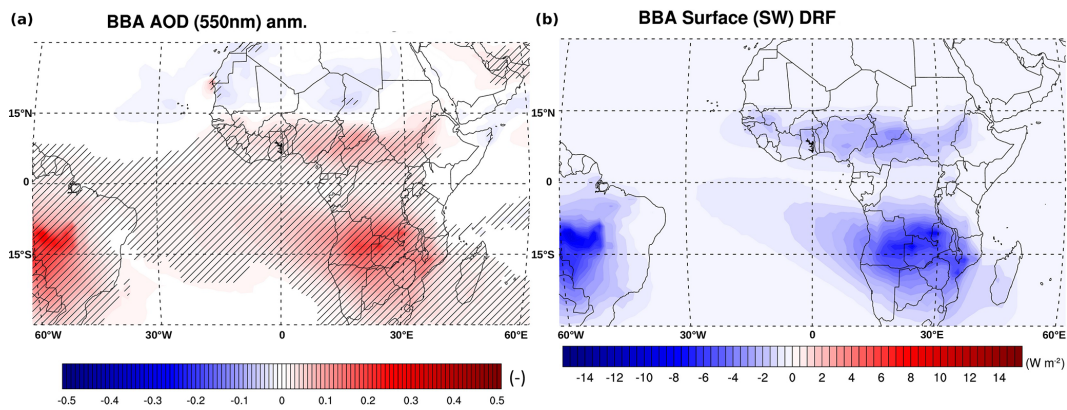


**Figure A9.** Averaged (1990–2014) seasonal (SON) anomaly of (a) BBA optical depth (at 550 nm; hatching indicates regions with a significant effect at the 0.05 level – Wilk test) and (b) effective SW surface direct radiative forcing simulated by the CNRM-CM model.

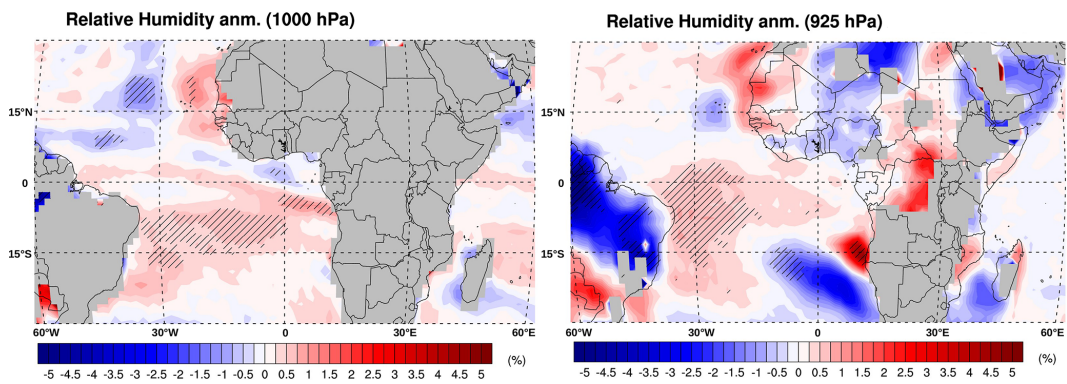


**Figure A10.** Averaged (1990–2014) seasonal (SON) anomaly of the relative humidity (%) at 1000 and 925 hPa. Hatching indicates regions with a significant effect at the 0.05 level (Wilk test).

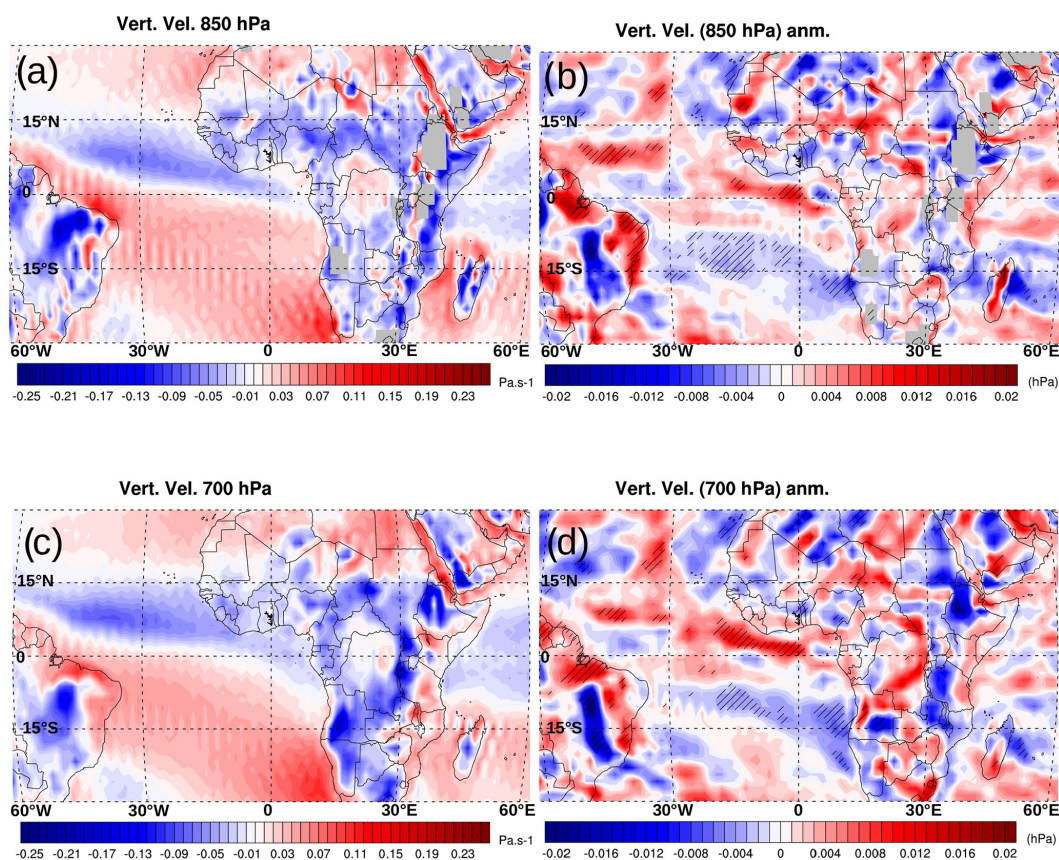


**Figure A11.** Averaged (1990–2014) seasonal (SON) vertical velocity at the vertical levels of 850 and 700 hPa (**a, c**,  $\text{Pa s}^{-1}$ ) and the corresponding anomalies (**b, d**,  $\text{Pa s}^{-1}$ ) simulated by the CNRM-CM model. Hatching indicates regions with a significant effect at the 0.05 level (Wilk test).

**Data availability.** This study relies entirely on publicly available data, which is available at: <https://doi.org/10.5281/zenodo.14002448> (Mallet et al., 2024). All the output files from ARPEGE-Climat simulations used in the present study are available on request.

**Author contributions.** MM, AV, PN and RR designed the modelling study and developed the analysis protocols. FS and TD contributed to the data analysis. All the authors reviewed the final manuscript.

**Competing interests.** The contact author has declared that none of the authors has any competing interests.

**Disclaimer.** Publisher’s note: Copernicus Publications remains neutral with regard to jurisdictional claims made in the text, published maps, institutional affiliations, or any other geographical representation in this paper. While Copernicus Publications makes every effort to include appropriate place names, the final responsibility lies with the authors.

**Special issue statement.** This article is part of the special issue “New observations and related modelling studies of the aerosol–cloud–climate system in the Southeast Atlantic and southern Africa regions (ACP/AMT inter-journal SI)”. It is not associated with a conference.

**Acknowledgements.** We are grateful to the CNRM climate group that develops and supports the CNRM climate model used in the present work. This work also benefited from Météo-France HPC resources.

**Review statement.** This paper was edited by Tak Yamaguchi and reviewed by two anonymous referees.

## References

- Ajoku, O., Norris, J., and Miller, A.: Observed monsoon precipitation suppression caused by anomalous interhemispheric aerosol transport, *Clim. Dynam.*, 54, 1077–1091, <https://doi.org/10.1007/s00382-019-05046-y>, 2019.
- Allen, R., Amiri-Farahani, A., Lamarque, J., Smith, C., Shindell, D., Hassan, T., and Chung, C.: Observationally constrained aerosol-cloud semi-direct effects, *npj Clim. Atmos. Sci.*, 2, 16, <https://doi.org/10.1038/s41612-019-0073-9>, 2019.
- Balkanski, Y., Bonnet, R., Boucher, O., Checa-Garcia, R., and Servonnat, J.: Better representation of dust can improve climate models with too weak an African monsoon, *Atmos. Chem. Phys.*, 21, 11423–11435, <https://doi.org/10.5194/acp-21-11423-2021>, 2021.
- Baró Pérez, A., Diamond, M. S., Bender, F. A.-M., Devasthale, A., Schwarz, M., Savre, J., Tonttila, J., Kokkola, H., Lee, H., Painemal, D., and Ekman, A. M. L.: Comparing the simulated influence of biomass burning plumes on low-level clouds over the southeastern Atlantic under varying smoke conditions, *Atmos. Chem. Phys.*, 24, 4591–4610, <https://doi.org/10.5194/acp-24-4591-2024>, 2024.
- Belamari, S. and Pirani, A.: Validation of the optimal heat and momentum fluxes using the ORCA2LIM global oceanic model. In: *Marine Environment and Security for the European Area Integrated Project (MERSEA IP)*, deliverable, CNRM, Toulouse, D.4.1.3, 88 pp., 2007.
- Brient, F., Roehrig, R., and Voldoire, A.: Evaluating marine stratocumulus clouds in the CNRM-CM6-1 model using short-term hindcasts, *J. Adv. Model. Earth Sy.*, 11, 127–148, <https://doi.org/10.1029/2018MS001461>, 2019.
- Chaboureaud, J.-P., Labbouz, L., Flamant, C., and Hodzic, A.: Acceleration of the southern African easterly jet driven by the radiative effect of biomass burning aerosols and its impact on transport during AEROCLO-sA, *Atmos. Chem. Phys.*, 22, 8639–8658, <https://doi.org/10.5194/acp-22-8639-2022>, 2022.
- Chaboureaud, J.-P., Labbouz, L., Flamant, C., and Hodzic, A.: Acceleration of the southern African easterly jet driven by the radiative effect of biomass burning aerosols and its impact on transport during AEROCLO-sA, *Atmos. Chem. Phys.*, 22, 8639–8658, <https://doi.org/10.5194/acp-22-8639-2022>, 2022.
- Che, H., Stier, P., Gordon, H., Watson-Parris, D., and Deaconu, L.: Cloud adjustments dominate the overall negative aerosol radiative effects of biomass burning aerosols in UKESM1 climate model simulations over the south-eastern Atlantic, *Atmos. Chem. Phys.*, 21, 17–33, <https://doi.org/10.5194/acp-21-17-2021>, 2021.
- Cochrane, S. P., Schmidt, K. S., Chen, H., Pilewskie, P., Kittelman, S., Redemann, J., LeBlanc, S., Pistone, K., Segal Rozenhaimer, M., Kacenelenbogen, M., Shinozuka, Y., Flynn, C., Ferrare, R., Burton, S., Hostetler, C., Mallet, M., and Zuidema, P.: Biomass burning aerosol heating rates from the ORACLES (Observations of Aerosols above Clouds and their interactions) 2016 and 2017 experiments, *Atmos. Meas. Tech.*, 15, 61–77, <https://doi.org/10.5194/amt-15-61-2022>, 2022.
- Decharme, B., Delire, C., Minvielle, M., Colin, J., Vergnes, J.-P., Alias, A., Saint-Martin, D., Séférian, R., Sénéci, S., and Voldoire, A.: Recent Changes in the ISBA-CTRIP Land Surface System for Use in the CNRM-CM6 Climate Model and in Global Off-Line Hydrological Applications, *J. Adv. Model. Earth Sy.*, 11, 1207–1252, <https://doi.org/10.1029/2018MS001545>, 2019.
- de Graaf, M., Bellouin, N., Tilstra, L., Haywood, J., and Stammes, P.: Aerosol direct radiative effect of smoke over clouds over the southeast Atlantic Ocean from 2006 to 2009, *Geophys. Res. Lett.*, 41, 7723–7730, <https://doi.org/10.1002/2014GL061103>, 2014.
- Denjean, C., Bourrienne, T., Burnet, F., Mallet, M., Maury, N., Colomb, A., Dominutti, P., Brito, J., Dupuy, R., Sellegri, K., Schwarzenboeck, A., Flamant, C., and Knippertz, P.: Overview of aerosol optical properties over southern West Africa from DACCIWA aircraft measurements, *Atmos. Chem. Phys.*, 20, 4735–4756, <https://doi.org/10.5194/acp-20-4735-2020>, 2020.
- Dentener, F., Kinne, S., Bond, T., Boucher, O., Cofala, J., Geroso, S., Ginoux, P., Gong, S., Hoelzemann, J. J., Ito, A., Marelli, L., Penner, J. E., Putaud, J.-P., Textor, C., Schulz, M., van der Werf, G. R., and Wilson, J.: Emissions of primary aerosol and precursor gases in the years 2000 and 1750 prescribed data-sets for AeroCom, *Atmos. Chem. Phys.*, 6, 4321–4344, <https://doi.org/10.5194/acp-6-4321-2006>, 2006.
- Diamond, M. S., Saide, P. E., Zuidema, P., Ackerman, A. S., Doherty, S. J., Fridlind, A. M., Gordon, H., Howes, C., Kazil, J., Yamaguchi, T., Zhang, J., Feingold, G., and Wood, R.: Cloud adjustments from large-scale smoke–circulation interactions strongly modulate the southeastern Atlantic stratocumulus-to-cumulus transition, *Atmos. Chem. Phys.*, 22, 12113–12151, <https://doi.org/10.5194/acp-22-12113-2022>, 2022.
- Doherty, S. J., Saide, P. E., Zuidema, P., Shinozuka, Y., Ferrada, G. A., Gordon, H., Mallet, M., Meyer, K., Painemal, D., Howell, S. G., Freitag, S., Dobracki, A., Podolske, J. R., Burton, S. P., Ferrare, R. A., Howes, C., Nabat, P., Carmichael, G. R., da Silva, A., Pistone, K., Chang, I., Gao, L., Wood, R., and Redemann, J.: Modeled and observed properties related to the direct aerosol radiative effect of biomass burning aerosol over the southeastern Atlantic, *Atmos. Chem. Phys.*, 22, 1–46, <https://doi.org/10.5194/acp-22-1-2022>, 2022.
- Drugé, T., Nabat, P., Mallet, M., and Somot, S.: Model simulation of ammonium and nitrate aerosols distribution in the Euro-Mediterranean region and their radiative and climatic effects over 1979–2016, *Atmos. Chem. Phys.*, 19, 3707–3731, <https://doi.org/10.5194/acp-19-3707-2019>, 2019.
- Drugé, T., Nabat, P., Mallet, M., Michou, M., Rémy, S., and Dubovik, O.: Modeling radiative and climatic effects of brown carbon aerosols with the ARPEGE-Climat global climate model, *Atmos. Chem. Phys.*, 22, 12167–12205, <https://doi.org/10.5194/acp-22-12167-2022>, 2022.
- Eyring, V., Bony, S., Meehl, G. A., Senior, C. A., Stevens, B., Stouffer, R. J., and Taylor, K. E.: Overview of the Coupled Model Intercomparison Project Phase 6 (CMIP6) experimental design and organization, *Geosci. Model Dev.*, 9, 1937–1958, <https://doi.org/10.5194/gmd-9-1937-2016>, 2016.
- Feng, N. and Christopher, S.: Measurement-based estimates of direct radiative effects of absorbing aerosols above clouds, *J. Geophys. Res.-Atmos.*, 120, 6908–6921, <https://doi.org/10.1002/2015JD023252>, 2015.
- Fouquart, Y. and Bonnel, B.: Computations of solar heating of the earth's atmosphere- A new parameterization, *Beitraege zur Physik der Atmosphaere*, 53, 35–62, 1980.

- Giorgi, F., Coppola, E., Giuliani, G., Ciarlo, J., Pichelli, E., Nogherotto, R., Raffaele, F., Malguzzi, P., Davolio, S., Stocchi, P., and Drofa, O.: The fifth generation regional climate modeling system, RegCM5: Description and illustrative examples at parameterized convection and convection-permitting resolutions, *J. Geophys. Res.*, 128, 6, <https://doi.org/10.1029/2022JD038199>, 2023.
- Gordon, H., Field, P. R., Abel, S. J., Dalvi, M., Grosvenor, D. P., Hill, A. A., Johnson, B. T., Miltenberger, A. K., Yoshioka, M., and Carslaw, K. S.: Large simulated radiative effects of smoke in the south-east Atlantic, *Atmos. Chem. Phys.*, 18, 15261–15289, <https://doi.org/10.5194/acp-18-15261-2018>, 2018.
- Herbert, R. J., Bellouin, N., Highwood, E. J., and Hill, A. A.: Diurnal cycle of the semi-direct effect from a persistent absorbing aerosol layer over marine stratocumulus in large-eddy simulations, *Atmos. Chem. Phys.*, 20, 1317–1340, <https://doi.org/10.5194/acp-20-1317-2020>, 2020.
- Holanda, B., Franco, M., Walter, D., Artaxo, P., Carbone, S., Cheng, Y., Chowdhury, S., Ditas, F., Gysel-Beer, M., Klimach, T., Kremper, L., Krüger, O., Lavric, J., Lelieveld, J., Ma, C., Machado, L., Modini, R., Morais, F., Pozzer, A., Saturno, J., Su, H., Wendisch, M., Wolff, S., Pöhlker, M., Andreae, M., Pöschl, U., and Pöhlker, C.: African biomass burning affects aerosol cycling over the Amazon, *Commun. Earth Environ.*, 4, 154, <https://doi.org/10.1038/s43247-023-00795-5>, 2023.
- Jiang, Y., Yang, X.-Q., Liu, X., Qian, Y., Zhang, K., Wang, M., Li, F., Wang, Y., and Lu, Z.: Impacts of Wildfire Aerosols on Global Energy Budget and Climate: The Role of Climate Feedbacks, *J. Climate*, 33, 3351–3366, <https://doi.org/10.1175/JCLI-D-19-0572.1>, 2020.
- Johnson, B., Shine, K., and Forster, P.: The semi-direct aerosol effect: Impact of absorbing aerosols on marine stratocumulus, *Q. J. Roy. Meteor. Soc.*, 130, 1407–1422, <https://doi.org/10.1256/qj.03.61>, 2004.
- Johnson, B. T., Haywood, J. M., Langridge, J. M., Darbyshire, E., Morgan, W. T., Szpek, K., Brooke, J. K., Marengo, F., Coe, H., Artaxo, P., Longo, K. M., Mulcahy, J. P., Mann, G. W., Dalvi, M., and Bellouin, N.: Evaluation of biomass burning aerosols in the HadGEM3 climate model with observations from the SAMBBA field campaign, *Atmos. Chem. Phys.*, 16, 14657–14685, <https://doi.org/10.5194/acp-16-14657-2016>, 2016.
- Kacenelenbogen, M. S., Vaughan, M. A., Redemann, J., Young, S. A., Liu, Z., Hu, Y., Omar, A. H., LeBlanc, S., Shinozuka, Y., Livingston, J., Zhang, Q., and Powell, K. A.: Estimations of global shortwave direct aerosol radiative effects above opaque water clouds using a combination of A-Train satellite sensors, *Atmos. Chem. Phys.*, 19, 4933–4962, <https://doi.org/10.5194/acp-19-4933-2019>, 2019.
- Klein, S. and Hartmann, D.: The seasonal cycle of low stratiform clouds, *J. Climate*, 6, 1588–1606, [https://doi.org/10.1175/1520-0442\(1993\)006<1587:TSCOLS>2.0.CO;2](https://doi.org/10.1175/1520-0442(1993)006<1587:TSCOLS>2.0.CO;2), 1993.
- Lu, Z., Liu, X., Zhang, Z., Zhao, C., Meyer, K., Rajapakshe, C., Wu, C., Yang, Z., and Penner, J.: Biomass smoke from southern Africa can significantly enhance the brightness of stratocumulus over the south-eastern Atlantic Ocean, *P. Natl Acad. Sci. USA*, 115, 2924–2929, <https://doi.org/10.1073/pnas.1713703115>, 2018.
- Lu, Z., Liu, X., Zhang, Z., Zhao, C., Meyer, K., Rajapakshe, C., Wu, C., Yang, Z., and Penner, J.: Can biomass burning aerosol induced surface cooling be amplified through sea surface temperature-cloud feedback over the Southeast Atlantic?, *Geophys. Res. Letters*, 50, e2022GL101377, <https://doi.org/10.1029/2022GL101377>, 2023.
- Madec, G., Bourdallé-Badie, R., Bouttier, P., Bricaud, C., Bruciaferri, D., Calvert, D., Chanut, J., Clementi, E., Coward, A., Delrosso, D., Ethé, C., Flavoni, S., Graham, T., Harle, J., Iovino, D., Lea, D., Lévy, C., Lovato, T., Martin, N., Masson, S., Mocavero, S., Paul, J., Rousset, C., Storkey, D., Storto, A., and Vancoppenolle, M.: NEMO ocean engine (Version v3.6), Notes Du Pôle De Modélisation De L'institut Pierre-simon Laplace (IPSL), Zenodo, <https://doi.org/10.5281/zenodo.1472492>, 2017.
- Mallet, M., Nabat, P., Zuidema, P., Redemann, J., Sayer, A. M., Stengel, M., Schmidt, S., Cochrane, S., Burton, S., Ferrare, R., Meyer, K., Saide, P., Jethva, H., Torres, O., Wood, R., Saint Martin, D., Roehrig, R., Hsu, C., and Formenti, P.: Simulation of the transport, vertical distribution, optical properties and radiative impact of smoke aerosols with the ALADIN regional climate model during the ORACLES-2016 and LASIC experiments, *Atmos. Chem. Phys.*, 19, 4963–4990, <https://doi.org/10.5194/acp-19-4963-2019>, 2019.
- Mallet, M., Solmon, F., Nabat, P., Elguindi, N., Waquet, F., Bouniol, D., Sayer, A. M., Meyer, K., Roehrig, R., Michou, M., Zuidema, P., Flamant, C., Redemann, J., and Formenti, P.: Direct and semi-direct radiative forcing of biomass-burning aerosols over the southeast Atlantic (SEA) and its sensitivity to absorbing properties: a regional climate modeling study, *Atmos. Chem. Phys.*, 20, 13191–13216, <https://doi.org/10.5194/acp-20-13191-2020>, 2020.
- Mallet, M., Nabat, P., Johnson, B., Michou, M., Haywood, J., Chen, C., and Dubovik, O.: Climate models generally underrepresent the warming by Central Africa biomass-burning aerosols over the Southeast Atlantic, *Sci. Adv.*, 7, eabg9998, <https://doi.org/10.1126/sciadv.abg9998>, 2021.
- Mallet, M., Voldoire, A., Solmon, F., Nabat, P., Drugé, T., and Roehrig, R.: CNRM-CM global model outputs for Biomass Burning aerosols study, Zenodo [data set], <https://doi.org/10.5281/zenodo.14002448>, 2024.
- Maranan, M., Fink, A., and Knippertz, P.: Rainfall types over southern West Africa: Objective identification, climatology and synoptic environment, *Q. J. Roy. Meteor. Soc.*, 144, 1628–1648, <https://doi.org/10.1002/qj.3345>, 2018.
- Meyer, K., Platnick, S., Oreopoulos, L., and Lee, D.: Estimating the direct radiative effect of absorbing aerosols overlying marine boundary layer clouds in the southeast Atlantic using MODIS and CALIOP, *J. Geophys. Res.-Atmos.*, 118, 4801–4815, <https://doi.org/10.1002/jgrd.50449>, 2013.
- Michou, M., Nabat, P., and Saint-Martin, D.: Development and basic evaluation of a prognostic aerosol scheme (v1) in the CNRM Climate Model CNRM-CM6, *Geosci. Model Dev.*, 8, 501–531, <https://doi.org/10.5194/gmd-8-501-2015>, 2015.
- Michou, M., Nabat, P., Saint-Martin, D., Bock, J., Decharme, B., Mallet, M., Roehrig, R., Séférian, R., Sénési, S., and Voldoire, A.: Present-day and historical aerosol and ozone characteristics in CNRM CMIP6 simulations, *J. Adv. Model. Earth Sy.*, 12, e2019MS001816, <https://doi.org/10.1029/2019MS001816>, 2020.
- Mlawer, E. J., Taubman, S. J., Brown, P. D., Iacono, M. J., and Clough, S. A.: Radiative transfer for inhomogeneous atmo-

- spheres: RRTM, a validated correlated-k model for the longwave, *J. Geophys. Res.*, 102, 16663–16682, 1997.
- Morcrette, J.-J., Barker, H. W., Cole, J. N. S., Iacono, M. J., and Pincus, R.: Impact of a New Radiation Package, McRad, in the ECMWF Integrated Forecasting System, *Mon. Weather Rev.*, 136, 4773–4798, <https://doi.org/10.1175/2008MWR2363.1>, 2008.
- Mulcahy, J. P., Johnson, C., Jones, C. G., Povey, A. C., Scott, C. E., Sellar, A., Turnock, S. T., Woodhouse, M. T., Abraham, N. L., Andrews, M. B., Bellouin, N., Browse, J., Carslaw, K. S., Dalvi, M., Folberth, G. A., Glover, M., Grosvenor, D. P., Hardacre, C., Hill, R., Johnson, B., Jones, A., Kipling, Z., Mann, G., Mollard, J., O'Connor, F. M., Palmiéri, J., Reddington, C., Rumbold, S. T., Richardson, M., Schutgens, N. A. J., Stier, P., Stringer, M., Tang, Y., Walton, J., Woodward, S., and Yool, A.: Description and evaluation of aerosol in UKESM1 and HadGEM3-GC3.1 CMIP6 historical simulations, *Geosci. Model Dev.*, 13, 6383–6423, <https://doi.org/10.5194/gmd-13-6383-2020>, 2020.
- Myhre, G., Forster, P., Samset, B., Hodnebrog, Å., Sillmann, J., Aalbergstjø, S., Andrews, T., Boucher, O., Faluvegi, G., Fläschner, D., Iversen, T., Kasoar, M., Kharin, V., Kirkevåg, A., Lamarque, J.-F., Olivié, D., Richardson, T., Shindell, D., Shine, K. P., Stjern, C. W., Takemura, T., Voulgarakis, A., and Zwiers, F.: PDRMIP: A Precipitation Driver and Response Model Intercomparison Project-Protocol and Preliminary Results, *B. Am. Meteor. Soc.*, 98, 1185–1198, <https://doi.org/10.1175/BAMS-D-16-0019.1>, 2017.
- Nabat, P., Somot, S., Cassou, C., Mallet, M., Michou, M., Bouniol, D., Decharme, B., Drugé, T., Roehrig, R., and Saint-Martin, D.: Modulation of radiative aerosols effects by atmospheric circulation over the Euro-Mediterranean region, *Atmos. Chem. Phys.*, 20, 8315–8349, <https://doi.org/10.5194/acp-20-8315-2020>, 2020.
- O’Gorman, P., Allan, R., Byrne, M., and Previdi, M.: Energetic constraints on precipitation under climate change, *Surv. Geophys.*, 33, 585–608, <https://doi.org/10.1007/s10712-011-9159-6>, 2012.
- Persad, G. G.: The dependence of aerosols’ global and local precipitation impacts on the emitting region, *Atmos. Chem. Phys.*, 23, 3435–3452, <https://doi.org/10.5194/acp-23-3435-2023>, 2023.
- Redemann, J., Wood, R., Zuidema, P., Doherty, S. J., Luna, B., LeBlanc, S. E., Diamond, M. S., Shinozuka, Y., Chang, I. Y., Ueyama, R., Pfister, L., Ryoo, J.-M., Dobracki, A. N., da Silva, A. M., Longo, K. M., Kacenelenbogen, M. S., Flynn, C. J., Pistone, K., Knox, N. M., Piketh, S. J., Haywood, J. M., Formenti, P., Mallet, M., Stier, P., Ackerman, A. S., Bauer, S. E., Fridlind, A. M., Carmichael, G. R., Saide, P. E., Ferrada, G. A., Howell, S. G., Freitag, S., Cairns, B., Holben, B. N., Knobelspiesse, K. D., Tanelli, S., L’Ecuyer, T. S., Dzambo, A. M., Sy, O. O., McFarquhar, G. M., Poellot, M. R., Gupta, S., O’Brien, J. R., Nenes, A., Kacarab, M., Wong, J. P. S., Small-Griswold, J. D., Thornhill, K. L., Noone, D., Podolske, J. R., Schmidt, K. S., Pilewskie, P., Chen, H., Cochrane, S. P., Sedlacek, A. J., Lang, T. J., Stith, E., Segal-Rozenhaimer, M., Ferrare, R. A., Burton, S. P., Hostetler, C. A., Diner, D. J., Seidel, F. C., Platnick, S. E., Myers, J. S., Meyer, K. G., Spangenberg, D. A., Maring, H., and Gao, L.: An overview of the ORACLES (ObSERvations of Aerosols above CLouds and their intERactionS) project: aerosol–cloud–radiation interactions in the southeast Atlantic basin, *Atmos. Chem. Phys.*, 21, 1507–1563, <https://doi.org/10.5194/acp-21-1507-2021>, 2021.
- Roehrig, R., Beau, I., Saint-Martin, D., Alias, A., Decharme, B., Guérémy, J.-F., Voldoire, A., Abdel-Lathif, A. Y., Bazile, E., Belamari, S., Blein, S., Bouniol, D., Bouteloup, Y., Cattiaux, J., Chauvin, F., Chevallier, M., Colin, J., Douville, H., Marquet, P., Michou, M., Nabat, P., Oudar, T., Peyrillé, P., Piriou, J.-M., Salas y Mélia, D., Sférian, R., and Sénési, S.: The CNRM Global Atmosphere Model ARPEGE-Climat 6.3: Description and Evaluation, *J. Adv. Model. Earth Sy.*, 12, e2020MS002075, <https://doi.org/10.1029/2020MS002075>, 2020.
- Rémy, S., Kipling, Z., Huijnen, V., Flemming, J., Nabat, P., Michou, M., Ades, M., Engelen, R., and Peuch, V.-H.: Description and evaluation of the tropospheric aerosol scheme in the Integrated Forecasting System (IFS-AER, cycle 47R1) of ECMWF, *Geosci. Model Dev.*, 15, 4881–4912, <https://doi.org/10.5194/gmd-15-4881-2022>, 2022.
- Sakaeda, N., Wood, R., and Rasch, P.: Direct and semi-direct aerosol effects of southern African biomass burning aerosol, *J. Geophys. Res.*, 116, D12205, <https://doi.org/10.1029/2010JD015540>, 2011.
- Samset, B.: Aerosol absorption has an underappreciated role in historical precipitation change, *Commun. Earth Environ.*, 3, <https://doi.org/10.1038/s43247-022-00576-6>, 2022.
- Samset, B., Myhre, G., Forster, P., Hodnebrog, Ø., Andrews, T., Faluvegi, G., Fläschner, D., Kasoar, M., Kharin, V., Kirkevåg, A., Lamarque, J.-F., Olivié, D., Richardson, T., Shindell, D., Shine, K. P., Takemura, T., and Voulgarakis, A.: Fast and slow precipitation responses to individual climate forcings: A PDRMIP multimodel study, *Geophys. Res. Lett.*, 43, 2782–2791, <https://doi.org/10.1002/2016GL068064>, 2016.
- Shinozuka, Y., Kacenelenbogen, M. S., Burton, S. P., Howell, S. G., Zuidema, P., Ferrare, R. A., LeBlanc, S. E., Pistone, K., Brocardo, S., Redemann, J., Schmidt, K. S., Cochrane, S. P., Fenn, M., Freitag, S., Dobracki, A., Segal-Rosenheimer, M., and Flynn, C. J.: Daytime aerosol optical depth above low-level clouds is similar to that in adjacent clear skies at the same heights: airborne observation above the southeast Atlantic, *Atmos. Chem. Phys.*, 20, 11275–11285, <https://doi.org/10.5194/acp-20-11275-2020>, 2020.
- Slingo, J.: The development and verification of a cloud prediction scheme for the ECMWF model, *Q. J. Roy. Meteor. Soc.*, 113, 899–927, <https://doi.org/10.1002/qj.49711347710>, 1987.
- Solmon, F., Mallet, M., Elguindi, N., Giorgi, F., Zakey, A., and Konaré, A.: Dust aerosol impact on regional precipitation over western Africa, mechanisms and sensitivity to absorption properties, *Geophys. Res. Lett.*, 35, L24705, <https://doi.org/10.1029/2008GL035900>, 2008.
- Solmon, F., Elguindi, N., and Mallet, M.: Radiative and climatic effects of dust over West Africa, as simulated by a regional climate model, *Clim. Res.*, 52, 97–113, <https://doi.org/10.3354/cr01039>, 2012.
- Solmon, F., Elguindi, N., Mallet, M., Flamant, C., and Formenti, P.: West African monsoon precipitation impacted by the South Eastern Atlantic biomass burning aerosol outflow, *npj Clim. Atmos. Sci.*, 4, 54, <https://doi.org/10.1038/s41612-021-00210-w>, 2021.
- Sférian, R., Nabat, P., Michou, M., Saint-Martin, D., Voldoire, A., Colin, J., Decharme, B., Delire, C., Berthet, S., Chevallier, M., Sénési, S., Franchisteguy, L., Vial, J., Mallet, M., Joetzjer, E.,

- Geoffroy, O., Guérémy, J.-F., Moine, M.-P., Msadek, R., Ribes, A., Rocher, M., Roehrig, R., Salas-y Mélia, D., Sanchez, E., Terray, L., Valcke, S., Waldman, R., Aumont, O., Bopp, L., Deshayes, J., Éthé, C., and Madec, G.: Evaluation of CNRM Earth-System model, CNRM-ESM 2-1: role of Earth system processes in present-day and future climate, *J. Adv. Model. Earth Sy.*, 11, 4182–4227, <https://doi.org/10.1029/2019MS001791>, 2019.
- van der Werf, G. R., Randerson, J. T., Giglio, L., Collatz, G. J., Mu, M., Kasibhatla, P. S., Morton, D. C., DeFries, R. S., Jin, Y., and van Leeuwen, T. T.: Global fire emissions and the contribution of deforestation, savanna, forest, agricultural, and peat fires (1997–2009), *Atmos. Chem. Phys.*, 10, 11707–11735, <https://doi.org/10.5194/acp-10-11707-2010>, 2010.
- van Marle, M. J. E., Kloster, S., Magi, B. I., Marlon, J. R., Daniiau, A.-L., Field, R. D., Arneeth, A., Forrest, M., Hantson, S., Kehrwald, N. M., Knorr, W., Lasslop, G., Li, F., Mangenon, S., Yue, C., Kaiser, J. W., and van der Werf, G. R.: Historic global biomass burning emissions for CMIP6 (BB4CMIP) based on merging satellite observations with proxies and fire models (1750–2015), *Geosci. Model Dev.*, 10, 3329–3357, <https://doi.org/10.5194/gmd-10-3329-2017>, 2017.
- Voltaire, A., Saint-Martin, D., Sénési, S., Decharme, B., Alias, A., Chevallier, M., Colin, J., Guérémy, J.-F., Michou, M., Moine, M.-P., Nabat, P., Roehrig, R., Salas y Mélia, D., Séférian, R., Valcke, S., Beau, I., Belamari, S., Berthet, S., Cassou, C., Cattiaux, J., Deshayes, J., Douville, H., Ethé, C., Franchisteguy, L., Geoffroy, O., Lévy, C., Madec, G., Meurdesoif, Y., Msadek, R., Ribes, A., Sanchez-Gomez, E., Terray, L., and Waldman, R.: Evaluation of CMIP6 DECK experiments with CNRM-CM6-1, *J. Adv. Model. Earth Sy.*, 11, 2177–2213, <https://doi.org/10.1029/2019MS001683>, 2019.
- Wilcox, E. M.: Stratocumulus cloud thickening beneath layers of absorbing smoke aerosol, *Atmos. Chem. Phys.*, 10, 11769–11777, <https://doi.org/10.5194/acp-10-11769-2010>, 2010.
- Wilks, D.: On “field significance” and the false discovery rate, *J. Appl. Meteorol. Clim.*, 97, 1181–1189, <https://doi.org/10.1175/JAM2404.1>, 2006.
- Wilks, D.: “The stippling shows statistically significant grid points”: How research results are routinely overstated and overinterpreted, and what to do about it, *B. Am. Meteor. Soc.*, 97, 2263–2273, <https://doi.org/10.1175/BAMS-D-15-00267.1>, 2016.
- Wu, H., Taylor, J. W., Szpek, K., Langridge, J. M., Williams, P. I., Flynn, M., Allan, J. D., Abel, S. J., Pitt, J., Cotterell, M. I., Fox, C., Davies, N. W., Haywood, J., and Coe, H.: Vertical variability of the properties of highly aged biomass burning aerosol transported over the southeast Atlantic during CLARIFY-2017, *Atmos. Chem. Phys.*, 20, 12697–12719, <https://doi.org/10.5194/acp-20-12697-2020>, 2020.
- Zhao, S. and Suzuki, K.: Differing Impacts of Black Carbon and Sulfate Aerosols on Global Precipitation and the ITCZ Location via Atmosphere and Ocean Energy Perturbations, *J. Climate*, 32, 5567–5582, <https://doi.org/10.1175/JCLI-D-18-0616.1>, 2019.
- Zuidema, P., III, A. S., Flynn, C., Springston, S., Delgado, R., Zhang, J., Aiken, A., Koontz, A., and Muradyan, P.: The Ascension Island boundary layer in the remote southeast Atlantic is often smoky, *Gephys. Res. Lett.*, 45, 4456–4465, <https://doi.org/10.1002/2017GL076926>, 2018.